Martian dayglow as seen by the SPICAM UV spectrograph on Mars Express

François Leblanc, Jean-Yves Chaufray, Jean Lilensten, Olivier Witasse,
Jean-Loup Bertaux

Martian dayglow as seen by the SPICAM UV spectrograph on Mars Express

F. Leblanc,[1] J. Y. Chaufray,[1] J. Lilensten,[2] O. Witasse,[3] and J.-L. Bertaux[1]

[1] In this paper we describe measurements of the Martian dayglow obtained by SPICAM UV spectrograph on board Mars Express between October 2004 and March 2005. Typical spectra (of more than 24,000 individual spectra) display the main features of the dayglow already reported more than 30 years ago (Barth et al., 1971, 1972). The variations with altitude, solar zenith angle, and aerocentric longitude of the main emissions, namely, the CO Cameron band emissions ($a^3\Pi - X^1\Sigma^+$) from 180–260 nm, the CO_2^+ ultraviolet doublet ($B^2\Sigma^+ - X^2\Pi$) emission near 289 nm, the O resonance line at 130.4 nm, and the H Lyman alpha line at 121.6 nm, are detailed. The average temperature deduced from the CO_2^+ ($B^2\Sigma^+ - X^2\Pi$) emission scale height between 150 and 190 km is $T_\infty = 201 \pm 10$ K. The altitude of the peak of the dayglow emission varies from 120 km at low solar zenith angle ($\sim 30°$) up to 132 km at high solar zenith angle ($\sim 75°$). We also find 24 orbits in which the individual derived exospheric temperatures do not show significant variations with respect to solar zenith angle, aerocentric longitude, or longitude. The presence of crustal magnetic fields appears to correlate with a significant (~ 100 K) increase in exospheric temperature. We report also the first observations of emissions associated with the N_2 Vegard Kaplan band system in the Martian upper atmosphere.

1. Introduction

[2] The upper atmosphere/thermosphere/ionosphere (~ 100–250 km) of Mars is an intermediate dynamical region strongly coupled below to the lower atmosphere and above (via the ionosphere) to the solar wind [*Bougher et al.*, 2000]. Wave coupling of the lower and upper atmospheres of Mars is significant, with diurnal Kelvin waves and semi-diurnal tides providing significant temperature and wind perturbations in the lower thermosphere [*Bougher et al.*, 2000, 2001; *Forbes et al.*, 2002; *Wang and Nielsen*, 2004; *Withers et al.*, 2004] as well as nonmigrating tidal waves associated with the Martian topography [*Bougher et al.*, 2004]. Above 250 km, the solar wind picks up newly created ions (by photo-ionization, electron impact, or charge exchange) from the exosphere, resulting in mass loading. Such picked up ions are accelerated by the solar wind electric field of convection, and their resulting cycloidal motion allows them to either escape the Martian gravity field [*Lundin et al.*, 1989, 2004] or reimpact the Martian atmosphere, inducing additional atmospheric escape [*Luhmann and Kozyra*, 1991]. The Martian exosphere plays, therefore, a crucial role in the global escape of the Martian atmosphere, and thus to the history of water on Mars [*Chassefière and Leblanc*, 2004].

[3] Five methods have been used so far to probe the Martian upper atmosphere. In situ observations have been performed by descent probes: USSR Mars 6 [*Kerzhanovich*, 1977], Viking 1 and 2 [*Seiff and Kirk*, 1977; *Nier and McElroy*, 1977] and Pathfinder [*Schofield et al.*, 1997; *Magalhaes et al.*, 1999]. Accelerometer measurements of total density versus altitude have been performed during the aerobraking phase of Mars Global Surveyor (MGS) and Mars Odyssey between 110 and 170 km in altitude [*Keating et al.*, 1998, 2003]. Measurements of the orbital decay of MGS during its science phase orbits have been used to retrieve the density of the Martian atmosphere between 170 and 180 km in altitude [*Tracadas et al.*, 2001]. Radio occultation methods have been used to explore the Mars upper atmosphere and provide the electron density profile between 75 and 250 km in altitude [*Bougher et al.*, 2001, 2004; *Pätzold et al.*, 2005]. Finally, the fifth method is remote sensing of the airglow emission of the upper atmosphere [*Barth et al.*, 1971, 1972].

[4] From Earth orbit, the Extreme Ultraviolet Explorer (EUVE) has been used to observe He at 58.4 nm [*Krasnopolsky and Gladstone*, 2005], the Hubble Space Telescope (HST) has been used to observe D at 121.533 nm [*Krasnopolsky et al.*, 1998], and the Far Ultraviolet Spectroscopic Explorer (FUSE) has detected H_2, H, O, N, C, Ar, He, N^+, C^+, Ar^+ and bands of N_2 and CO [*Krasnopolsky and Feldman*, 2001, 2002]. Another high-quality far-ultraviolet (FUV) dayglow spectrum of Mars was obtained by the Hopkins Ultraviolet Telescope [*Feldman et al.*, 2000]. Four missions to Mars have had a UV spectrometer or spectrograph on board: the Mariner 6, 7 and 9 missions between 1969 and

[1]Service d'Aéronomie du CNRS/IPSL, Verrières-le-Buisson, France.
[2]Laboratoire de Planétologie de Grenoble, Grenoble, France.
[3]ESA-ESTEC, Noordwijk, Netherlands.
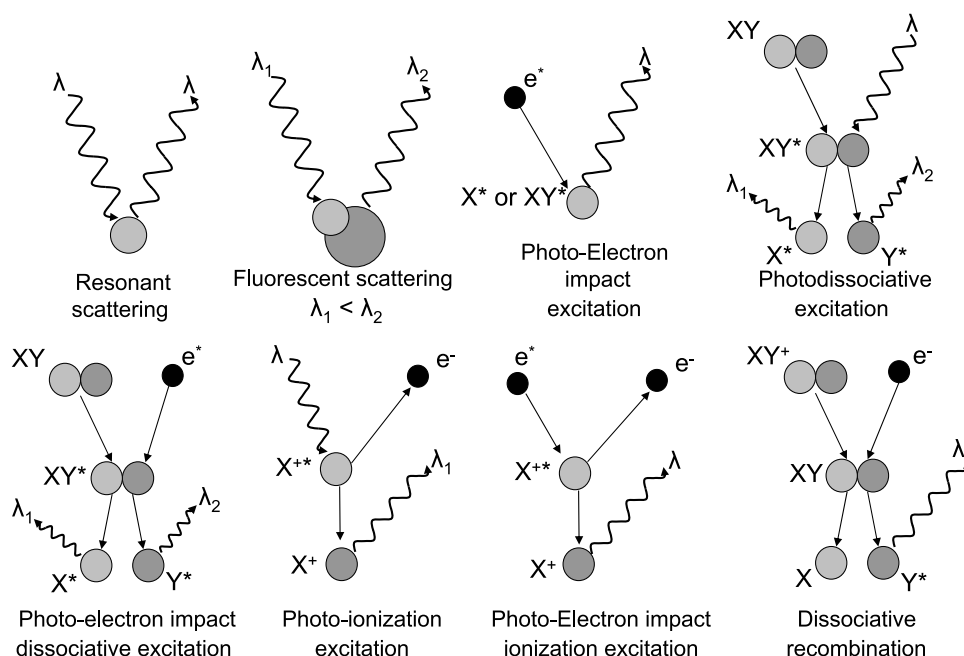
Figure 1. Scheme of the different mechanisms leading to the dayglow. λ, λ_1, and λ_2 are the wavelength of the incident or emitted photons. X and Y are atoms, and e^- is an electron; X^+ or Y^+ is for a positive ion, and X^*, Y^*, XY^*, or X^{+*} is an atom/molecule/ion in an excited state (adapted from *Paxton and Anderson* [1992]).

1971 [*Barth et al.*, 1971, 1972; *Stewart et al.*, 1972] and the still-operating Mars Express mission (MEX) with **SP**ectroscopy for the **I**nvestigation of the **C**haracteristics of the **A**tmosphere of **M**ars (SPICAM) on board. The Mariner 6, 7 and 9 UV spectrometers observed for the first time the main emission features of the Martian UV dayglow between 110 and 400 nm [*Barth et al.*, 1971, 1972]. Analyses of the Mariner data have shown that these airglow features are essentially produced by photon and photoelectron excitation of CO_2 between 100 and 200 km in altitude [*Fox and Dalgarno*, 1979; *Fox*, 1992; *Paxton and Anderson*, 1992]. Above 200 km, the main features are associated with H and O excited by resonantly scattered solar photons.

[5] In this paper, we present UV dayglow observations performed by the SPICAM UV spectrograph on Mars Express [*Bertaux et al.*, 2000, 2006]. The first section describes the general features of the Martian upper atmosphere that can be extracted from the dayglow, provides the coverage of the present set of observations (October 2004 to March 2005), and compares the average spectra observed by SPICAM with previously published observations. The second section describes the main characteristics of the Martian dayglow derived from this set of measurements. In Appendix A, we present a short description of the instrument, followed by a detailed description of the method used to analyze the data.

2. Observations

2.1. Expected Emission Lines

[6] Figure 1 shows schematically the primary mechanisms at work in the Martian UV dayglow.

[7] On the nightside, the SPICAM UVS has identified for the first time the main source of the Martian nightglow

[*Bertaux et al.*, 2005a] which is a chemiluminescence mechanism:

$$X + Y \rightarrow XY^* \rightarrow XY + h\nu$$

where the observed emission by SPICAM has been identified as the recombination glow of N and O atoms formed on the dayside and transported into the Martian nightside by the global Martian circulation.

[8] Table 1 provides the main emissions within SPICAM UV range (119–302 nm) that have been identified by previous UV spectrometers on the Martian orbiters Mariner 6, 7 and 9, but also from Earth orbiters (in particular using FUSE and HUT observatories). We also indicate the different mechanisms thought to be responsible for each emission (and the main authors of these identifications). We also indicate in Table 1 the typical intensity for each of these emissions according to previous published observations, even if these intensities often vary with respect to Solar Zenith Angle (SZA), Martian seasons, aerocentric longitude (Ls) and altitude.

[9] From the identification of the main mechanisms leading to the emissions observed in the Martian dayglow, *Barth et al.* [1971] concluded that "with the exception of the H I 121.6 nm, O I 130.4 nm lines and a portion of the CO_2^+ $A^1\Pi$ - $X^1\Sigma^+$ bands, all the emissions may be and probably are produced by action of solar photons and photoelectrons on carbon dioxide." Therefore the primary information regarding the Martian atmosphere that can be derived from these emissions is on the main constituent of the upper Martian atmosphere, carbon dioxide. We can also infer information about the production rate of ionospheric constituents of the Martian atmosphere. The main ionizable

Table 1. Dayglow Emissions Between 120 and 300 nm of the Martian Thermosphere/Ionosphere[a]

Line	λ, nm	Excitation Processes[b]	Intensity (Rayleigh)[c]	References
CO_2^+ $B^2\Sigma^+ - X^2\Pi$	288.3 289.6	PI (CO_2), EI (CO_2)	4×10^4 at 150 km 2×10^3 at 220 km	*Barth et al.* [1971, 1972] *Stewart et al.* [1972] *Fox and Dalgarno* [1979] *Witasse* [2000]
CO $a^3\Pi - X^1\Sigma^+$ Cameron band	190– 270	RS (CO), EE (CO), ED (CO_2) PD (CO_2), DR (CO_2^+)	2×10^4 at 200 km 5×10^5 at 110 km	*Barth et al.* [1971, 1972] *Stewart et al.* [1972] *Fox and Dalgarno* [1979] *Conway* [1981]
CO $A^1\Pi - X^1\Sigma^+$ 4P bands	128– 280	ED (CO_2), PD (CO_2), DR (CO_2^+) RS (CO)	3×10^3 at 100 km, 9×10^3 at 150 km 600 at 200 km	*Barth et al.* [1971] *Gutchek and Zipf* [1973] *Fox and Dalgarno* [1979, 1981] *Feldman et al.* [2000]
C	156.1	ED (CO_2), PD (CO_2), RS (C)	~50% of CI at 165.7 nm	*Barth et al.* [1971, 1972] *Fox and Dalgarno* [1979] *Feldman et al.* [2000]
C	165.7	ED (CO_2), PD (CO_2), RS (C)	800 at 100 1700 at 150 km 300 at 200 km	*Barth et al.* [1971, 1972] *Fox and Dalgarno* [1979] *Feldman et al.* [2000]
O	297.2	PD (CO_2), ED (CO_2), EE (O), DR (O_2^+)	2×10^4 at 120 km 10^3 at 190 km	*Barth et al.* [1971, 1972] *Fox and Dalgarno* [1979] *Witasse* [2000]
O	135.6	ED (CO_2), EE (O)	300 at 100 km, 400 at 150 km 100 at 200 km	*Barth et al.* [1971] *Strickland et al.* [1972] *Fox and Dalgarno* [1979] *Feldman et al.* [2000] *Witasse* [2000]
O	130.2 130.5 130.6	EE (CO_2 <200 km), RS (O)	600 at 110 km 500 at 200 km 10 at 700 km	*Barth et al.* [1971] *Strickland et al.* [1973] *Feldman et al.* [2000]
H	121.6	RS (H)	5000 at 200 km 200 at 24000 km	*Anderson and Hord* [1971] *Barth et al.* [1971, 1972]
N	120.0	RS (N)	~100 at 100 km	*Feldman et al.* [2000]
CO^+ $B^2\Sigma^+ - X^2\Sigma^+$	210–270	PI (CO_2), EI (CO_2)	Small fraction of CO Cameron band or not identified	*Stewart et al.* [1972] *Conway* [1981]

[a]Thermosphere/ionosphere: 100–200 km.

[b]The species in parentheses is the neutral atmospheric species leading to such an emission and excited by either Photo-ionization excitation (PI), Photo-Electron Impact Ionization excitation (EI), Photo-Electron impact excitation (EE), Photodissociative excitation (PD), Resonant scattering and fluorescent scattering (RS), Dissociative recombination (DR), or Photo-Electron impact dissociative excitation (ED).

[c]Integrated intensity over the wavelength range of the band for limb viewing for Mariner 6 and 7 [*Barth et al.*, 1971]. Mariner 6 and 7: 07/31/1969 to 08/05/1969, Ls = 200° (southern spring), zenith angle = 44°, 27°, and 0°, F10.7 = 167–188.

neutral constituent is CO_2, and the CO_2^+ ultraviolet doublet ($B^2\Sigma^+ - X^2\Pi$) near 289 nm is produced by photoionization/excitation of CO_2 by solar UV at $\lambda < 69$ nm. Another band system, the CO_2^+ Fox-Duffenback-Barker system ($A^2\Pi - X^2\Pi$) between 300 and 400 nm, is produced by a combination of photoionization/excitation of CO_2 and fluorescent scattering of sunlight by CO_2^+ ions. The SPICAM UV long wavelength cut-off is at 320 nm, which is enough to measure the (4,0) and (3,0) bands of the $A^2\Pi - X^2\Pi$ system. Unfortunately, above 302 nm the effective area of SPICAM is quite small, preventing a good signal/noise ratio (S/N ratio) for these two emission bands (Appendix A, section A2).

The H I 121.6 nm and O I 130.4 nm lines provide information on H and O in the thermosphere as well as in the exosphere, where these two species are thought to be the main constituents.

2.2. Orbital Coverage and Observation Geometry

[10] The orbital coverage of the Martian dayglow by the SPICAM UVS has been significantly limited by the need to rotate the spacecraft for each limb mode observation. Such a configuration is in conflict with the nadir pointed observation mode preferred by most of the instruments on MEX. Moreover, such limb observations are preferably done

around the pericenter of the orbit, which, for a significant part of the first two years of observations, occurred during Martian night.

[11] Table 2 provides the parameters for the 24 selected orbits during which the S/N ratio was sufficient to clearly identify most dayglow features. We exclude from this first collection 29 other limb dayglow observations obtained either with a low gain on the microchannel plate (MCP), or which displayed stray light features during part of the observation (Appendix A, section A2). Observations after September 2004 (whereas the first observation performed by SPICAM UVS was obtained in January 2004) have been selected because, before then, the gain of the MCP was never large enough to obtain a good S/N ratio for dayglow observations. Indeed, there was a risk that an intense signal measured when a large gain was applied might degrade the MCP. These early observations were used to characterize the expected atmospheric emissions and to define a dedicated set of operations for routine dayglow observations. Such special operations are defined such that the SPICAM UVS FOV shall not point below a predefined tangent altitude, avoiding in this way intense signals that could saturate the MCP. Typically, this tangent altitude was set at 80 km, since the solar flux reflected by Rayleigh or Mie scattering in the Martian upper atmosphere below this altitude was estimated to be large enough to saturate the detector with the high value of the gain we used.

[12] We divided the set of observations into two periods of Solar longitude; Ls = $100.95°$ – $130.1°$ (Figure 2a) and Ls = $138.56°$ – $171.02°$ (Figure 2b). The available observations of the Martian atmosphere at an altitude of 130 km above the surface (the expected altitude for the peak of the dayglow emission) cover a SZA range of $28°-65°$ for the first period and $30°-82°$ for the second period. As indicated in Table 2, all the measurements presented in this paper were obtained in the Martian afternoon.

[13] Figure 3 shows the coverage of the observations in term of east longitude and latitude overlaid on a map of the Martian crustal magnetic field (the radial component at 200 km altitude) as measured by Mars Global Surveyor [Acuña et al., 2001; Purucker et al., 2000]. The trajectory of MEX is parallel to the lines plotted in Figure 3. Since SPICAM points perpendicular to the velocity vector of MEX, its FOV is perpendicular to the lines plotted in Figure 3, which represent the track of the nearest point to Mars in the FOV. Several studies suggest the important affect of the crustal magnetic field on the Martian ionosphere [Mitchell et al., 2001; Brain et al., 2002; Krymskii et al., 2002]. Unfortunately, so far only one orbit (orbit 983) observed dayglow emissions above the strongest crustal magnetic field (near ~180° longitude in the southern hemisphere).

2.3. Comparison With Previous Observations

[14] The previous UV dayglow observations from Mars' orbit were obtained more than 30 years ago. Figures 4a and 4b show the average spectrum measured by the Mariner 9 UV spectrometer during 120 limb observations [Barth et al., 1972]. Using the measurements described in the previous section, we have constructed an average SPICAM UVS spectrum for the same altitude range (between 100 and 150 km in altitude). These observations by SPICAM and the Mariner 9 UV spectrometers were both obtained with

a spectral resolution of 1.5 nm (actually varying from 1 to 3 nm in the case of SPICAM UVS [see Bertaux et al., 2006, Figure 13]). The Mariner 9 observations were taken at a different aerocentric longitude (when Mars was closer to the Sun than in the case of SPICAM observations), at higher solar activity, and for generally smaller solar zenith angles. Overall, the SPICAM instrument is several hundred times more sensitive than the Mariner 9 instrument due to its multichannel detector.

[15] Within the spectral range 190 – 305 nm, corresponding to Figures 4a and 4c, Mariner 9 and SPICAM display the same features, namely, the CO Cameron band system ($a^3\Pi - X^1\Sigma^+$) between 190 nm and 270 nm, the CO_2^+ ultraviolet doublet ($B^2\Sigma^+ - X^2\Pi$) emission near 289 nm and the O ($^1S - {}^3P$) emission line at 297.2 nm. The relative brightness distribution of the different vibrational states within the Cameron band system observed by SPICAM is in good agreement with Mariner 9 observations, as well as the relative intensities of the CO_2^+ ($B^2\Sigma^+ - X^2\Pi$) emission at 289 nm and the total Cameron band system emission. Only the O ($^1S - {}^3P$) 297.2 nm emission appears to be significantly less intense with respect to the other emissions in the SPICAM data compared with the Mariner 9 data. Only one detailed analysis of the different emissions of the Martian UV dayglow has been published [Fox and Dalgarno, 1979]. This study was done in the conditions of Viking 1 measurements that is, for a solar zenith angle of 45°, low solar activity and an exospheric temperature ~200 K. In particular, these authors concluded that up to 90% of the $O(^1S)$ in the Martian atmosphere is produced by photodissociation of CO_2, whereas the CO_2^+ ($B^2\Sigma^+ - X^2\Pi$) ultraviolet doublet emission at 289 nm is produced essentially by photo-ionization of CO_2 with a small contribution due to electron impact ionization (~15%). The CO Cameron band system ($a^3\Pi - X^1\Sigma^+$) emission is produced by photon and electron impacts on CO_2 and by dissociative recombination of CO_2^+ (less than 15%). Unfortunately, there is no theoretical study on the way these emissions may vary with respect to the solar zenith angle. The (4,0) and (3,0) transitions of the CO_2^+ ($A^2\Pi - X^2\Pi$) band system between 300 and 310 nm may also be present in SPICAM spectrum (inside the gray part of Figure 4c), but unfortunately (as explained in section 3.1) with a small S/N ratio.

[16] Within the FUV spectral range of 110 – 200 nm, corresponding to Figures 4b and 4d, the spectra observed by the Mariner 9 UV spectrometer and SPICAM are composed of the same emissions: namely, the CO Fourth Positive (4P) ($A^1\Pi - X^1\Sigma^+$) band system, several C emission lines between 140 and 170 nm, the (2,0) vibrational band of the CO Cameron system, the atomic O emissions at 130.4 nm and 135.6 nm, and the H Lyman α emission at 121.6 nm. In Figure 5, we also provide another example of SPICAM measurement of the Martian dayglow between 110 and 180 nm obtained for SZA = 14 – 37°, Ls = 135 – 171° and between 140 – 150 km in altitude. Some differences exist between the SPICAM and Mariner 9 spectra, in particular the distributions of the emission intensities within 140 and 170 nm (e.g., the ratio between the 156.1 nm and 165.7 nm emission intensities). In the case of SPICAM, calibration of the 150 – 170 nm spectral range is complicated by the particular shape of the effective area curve between 150 and 170 nm combined

Table 2. MEX Orbits During Which Dayglow Observations are Used[a]

Date	Orbit	Bin Size	Solar Zenith Angle, deg	Longitude, deg	Latitude, deg	Altitude, km	Local Time, hour	Ls, deg	F10.7	T, K, From Cameron	T, K, From 289 nm	Altitude of the Cameron Peak, km	Intensity at the Cameron Peak, kR
2004 10 15	947	32	28 – 52 – 86	115 – 125 – 138	28N – 6S – 42S	393 – 77 – 370	14 – 15 – 16	100.9	89	266 – 221	197 – 163	116 – 111	152 – 88
2004 10 15	948	32	28 – 52 – 86	16 – 26.5 – 40	28 N – 5S – 41S	381 – 77 – 373	14 – 15 – 16	101.1	89	254 – 243	174 – 180	116 – 114	163 – 96
2004 10 16	952	32	27 – 51 – 85	343 – 353.5 – 7	29N – 5S – 41S	387 – 78 – 372	14 – 15 – 16	101.6	90.7	248 – 254	129 – 183	113 – 113	148 – 95
2004 10 17	958	32	37 – 49 – 84	120 – 124 – 137	11N – 4S – 40S	131 – 77 – 374	14 – 15 – 16	102.3	90.8	NA – 274	NA – 232	113 – 112	153 – 102
2004 10 18	959	32	26 – 49 – 83	15 – 26 – 39	30N – 4S – 40S	393 – 77 – 370	14 – 15 – 16	102.4	92.1	224 – 267	165 – 209	117 – 115	162 – 106
2004 10 24	981	32	23 – 44 – 78	12 – 24 – 37	34N – 0S – 36S	399 – 76 – 367	14 – 14.5 – 16	105.2	87.6	232 - 282	178 – 161	121 – 112	141 – 121
2004 10 24	983	32	22 – 43 – 78	175 – 187 – 201	34N – 0N – 35S	396 – 77 – 369	13.5 – 14.5 – 15.5	105.5	87.6	336 – 332	246 – 327	111 – 112	167 – 123
2004 11 08	1036	32	27 – 37 – 70	19 – 20 – 22	37N – 0N – 40S	418 – 77 – 462	13.8 – 14 – 14.3	112.2	133.4	299 – 246	280 – 207	115 – 110	203 – 179
2004 11 09	1039	32	27 – 37 – 70	85 – 85.8 – 86.4	38N – 0 – 40S	433 – 77 – 462	13.8 – 14 – 14.2	112.6	128.8	277 – 271	157 – 212	120 – 118	200 – 179
2004 12 16	1172	16	59 – 45 – 54	30 – 17 – 9	61N – 25N – 15S	403 – 76 – 487	16 – 15.2 – 14.8	130.1	89.7	230 – 234	188 – 185	120 – 113	168 – 135
2005 01 03	1234	32	66 – 41 – 35	72 – 47 – 38	70N – 35N – 5N	412 – 80 – 303	16.3 – 14.7 – 14.3	138.6	93	240 – 314	193 – 229	130 – 120	140 – 206
2005 01 11	1265	16	29.8 – 30.2	234.2 – 229.4	18N – 1N	200 – 470	14.1 – 13.8	142.9	94.2	NA	NA	NA	NA
2005 01 12	1267	16	71 – 41 – 29	84 – 45 – 32	74N – 41N – 2N	415 – 81 – 478	17 – 14.5 – 14	143.2	88	249 – 237	195 – 183	128 – 125	131 – 169
2005 01 13	1271	16	72 – 41 – 44	53 – 12 – 351	74N – 41N – 25S	418 – 82 – 1312	17 – 14 – 13	143.7	88.2	242 – 256	182 – 194	124 – 125	123 - 157
2005 01 17	1285	16	74 – 42 – 25	125 – 77 – 64	75N – 43N – 4N	418 – 83 – 476	17 – 14 – 13.5	145.7	87.5	239 – 241	160 – 202	132 – 129	125 – 171
2005 01 21	1298	16	76 – 43 – 22	296 – 240 – 225	76N – 46N – 7N	414 – 83 – 480	18 – 14 – 13	147.5	115.6	212 – 239	179 – 199	133 – 127	127 – 196
2005 01 27	1321	16	81 – 46 – 18	212 – 141 – 125	76N – 49N – 11N	421 – 85 – 474	19 – 14 – 13	151	132.5	232 – 233	164 – 175	132 – 127	131 – 213
2005 02 04	1349	16	66 – 39 – 28	265 – 267 – 266	75N – 41N – 8N	304 – 80 – 337	13.5 – 13.8 – 13.9	154.9	84.9	226 – 260	211 – 206	125 – 123	124 – 165
2005 02 04	1350	16	59 – 36 – 32	159 – 169 – 171	68N – 36N – 5N	266 – 77 – 316	13 – 13.9 – 14.1	155	84.9	198 – 290	142 – 283	127 – 121	159 – 192
2005 02 10	1371	16	90 – 53 – 14	6 – 272 – 250	73N – 57N – 20N	419 – 88 – 478	20 – 14 – 12.7	158.1	83	210 – 228	157 – 185	133 – 126	75 – 141
2005 02 22	1413	16	98 – 60 – 21	213 – 110 – 82	68N – 63N – 27N	429 – 90 – 471	20.8 – 14 – 12.3	164.3	121.7	219 – 287	182 – 230	136 – 128	72 – 178
2005 02 22	1414	16	98 – 61 – 21	115 – 13 – 343	67N – 63N – 27N	423 – 90 – 476	20.7 – 14 – 12.3	164.5	121.7	215 – 245	153 – 210	131 – 123	71 – 153
2005 02 26	1426	16	101 – 63 – 24	19 – 276 – 245	66N – 64N – 29N	435 – 90 – 465	20.9 – 14.1 – 12.2	166.3	98.5	242 – 236	165 – 208	131 – 130	57 – 153
2005 03 06	1457	16	106 – 68 – 31	218 – 117 – 79	61N – 68N – 34N	441 – 91 – 460	21 – 14.3 – 12	171	74.6	259 – 264	213 - 210	101 – 129	35 – 106

[a]The column "Bin Size" provides the number of CCD lines that have been summed to constitute each spatial bin. Solar Zenith Angle, Longitude, Latitude, Altitude (with a 2 km resolution), and Local Time are for Mars Nearest Point of the FOV of the UV spectrograph. The three values correspond to the beginning of the observation, to the sequence with the lowest altitude of the FOV, and to the end of the observation, except for Orbit 1265, where it corresponds to the beginning and end of the available data set. Ls is for solar longitude. F10.7 (10^{-22} W/m²/Hz) are calculated from daily average National Geophysics Data Center taking into account the relative positions of the Earth and Mars and the Sun rotation. The column "T, K, From Cameron" and "T, K, From 289 nm" are for the temperature of the upper atmosphere (above 140 km) derived from Cameron band system and the CO_2^{+} doublet at 289 nm emissions, respectively. Two values for the altitude (with a 5 km spatial resolution) and intensity of the Cameron band system emission are given which correspond to the peak observed during the downward and upward part of the orbit, respectively. NA, not available.
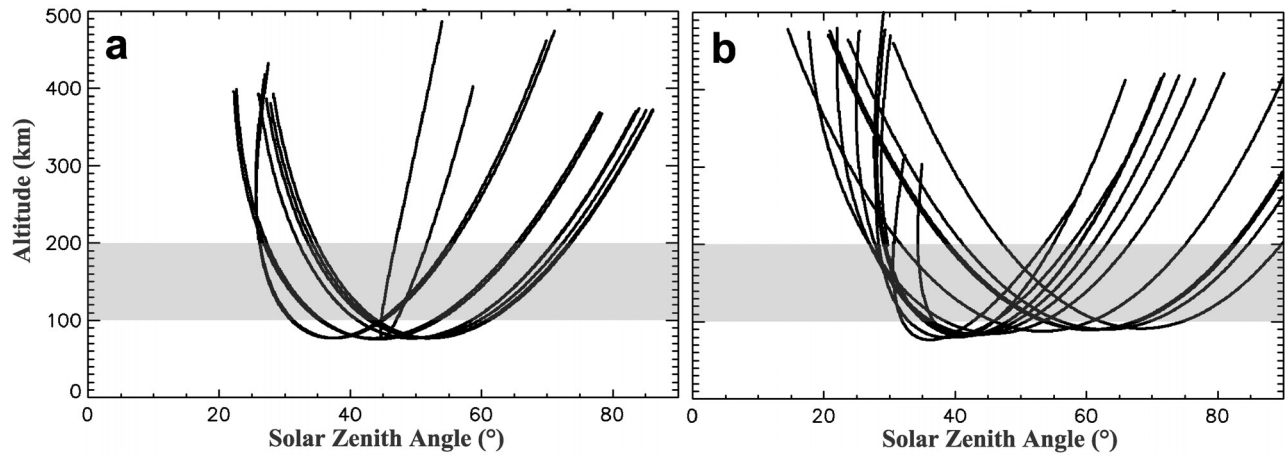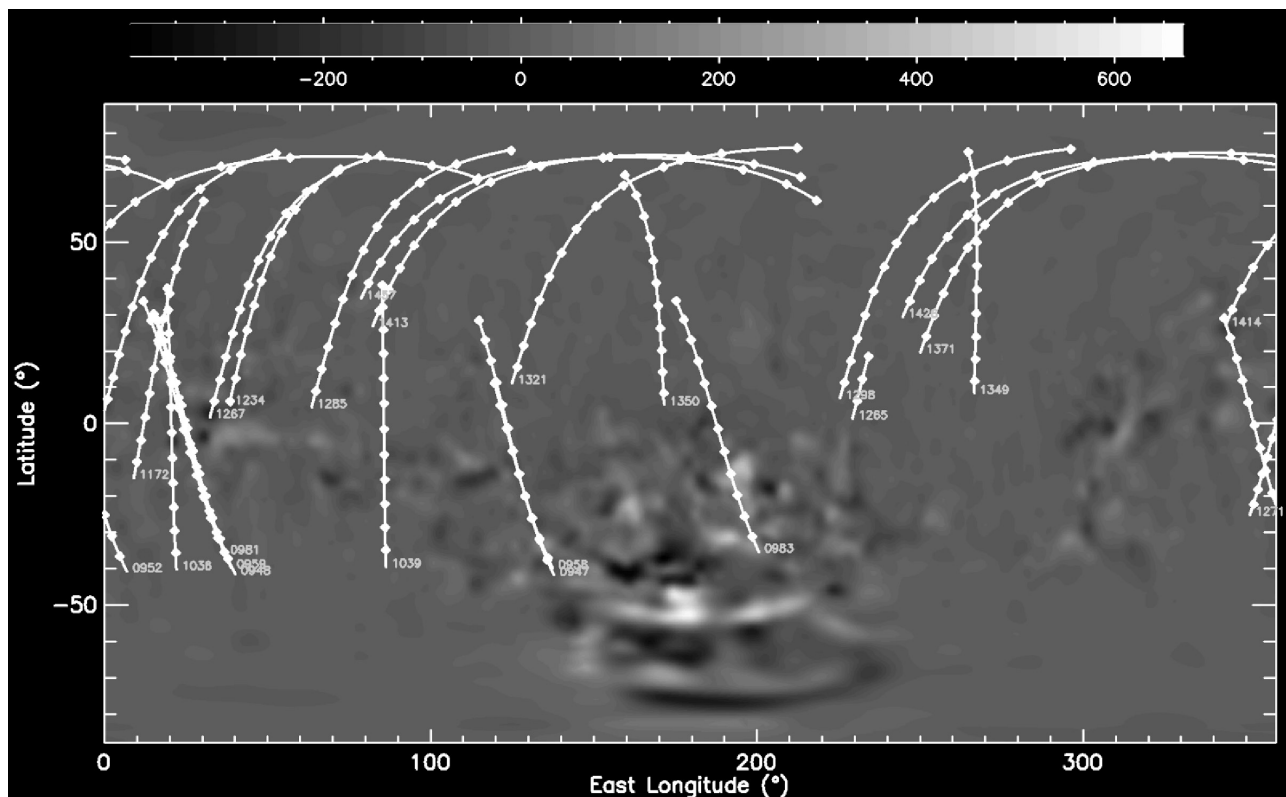
Figure 2. Traces of Mars Nearest Point of the FOV for the different period of observations selected from Table 2 plotted versus SZA and altitude. (a) Ten orbits during Ls = 100.95° − 130.1°. (b) Fourteen orbits during Ls = 138.56° − 171.02°.

with the SiO_2 entrance window (which has an edge at 170 nm; see Appendix A, section A1). This difficulty has been partially resolved by the observations of several well calibrated stars. The next year of SPICAM observations should reduce this uncertainty further, thanks to a forthcoming new set of star observations.

[17] *Feldman et al.* [2000] published an observation of the Martian dayglow from the Hopkins Ultraviolet Telescope (HUT) on board the ASTRO-2 shuttle mission in


Figure 3. Traces of Mars Nearest Point of the FOV for different periods of observation selected from Table 2, plotted versus latitude and east longitude and overlaid on a map of the radial component of the magnetic crustal field [*Purucker et al.*, 2000]. The horizontal scale bar plotted at the top of the figure provides field values in nT. We also indicate, close to the end of each trace, the number of the corresponding orbit.
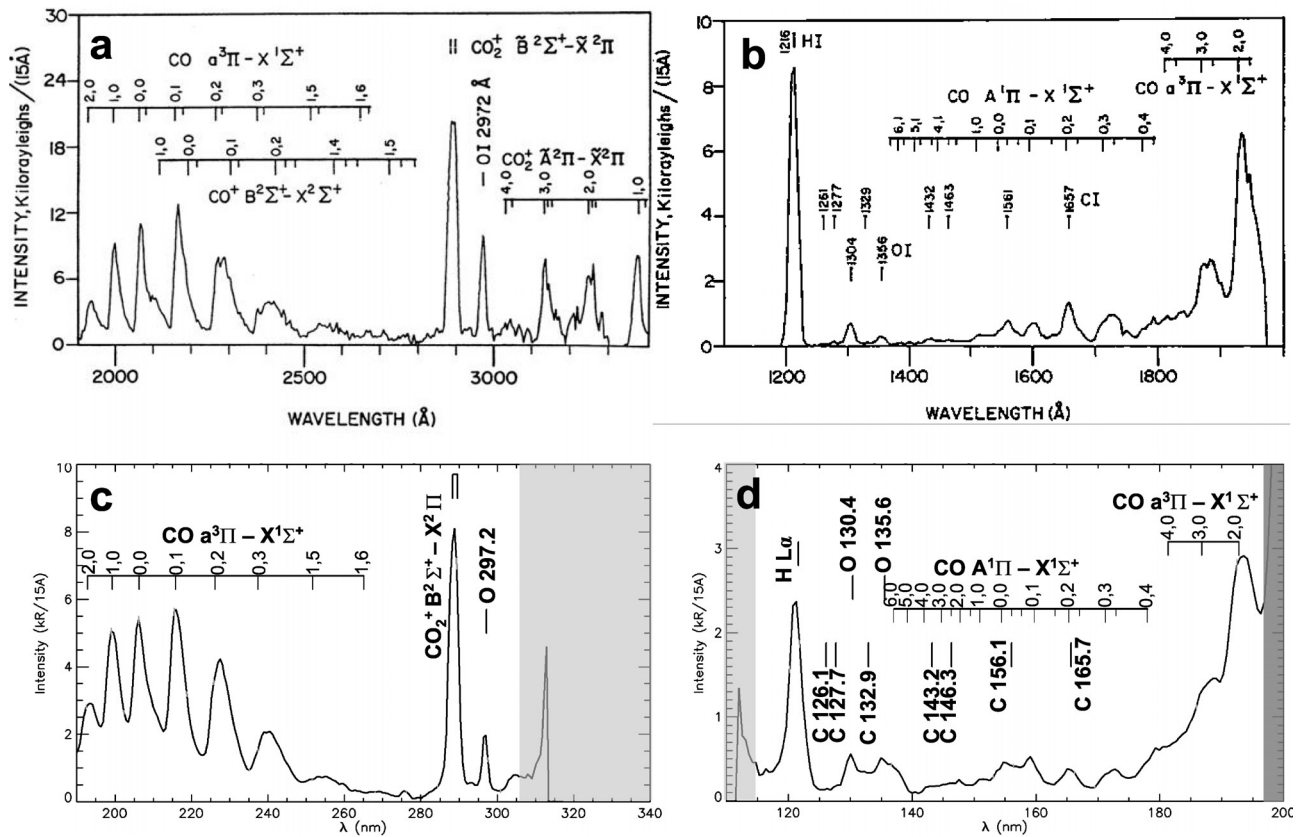
Figure 4. Comparison between SPICAM and Mariner 9 UV spectra [*Barth et al.*, 1972]. (a and b) Average of 120 Mariner 9 spectra obtained during solar activity F10.7 110–140 with a spectral resolution of 1.5 nm and between altitude 100 and 150 km at Ls = 312° with SZA = 7 − 23°. (c and d) Average of 730 SPICAM spectra obtained during solar activity F10.7 89 − 133 with a spectral resolution of 1.5 nm, between altitude of 100 and 150 km at Ls = 100 − 118° and SZA = 14 − 32°. Gray rectangles cover spectral region where the signal/noise ratio is small because of the size of the effective area except on the right side of Figure 4d, where it has been included to help a visual comparison with Figure 4b. (Plots displayed in Figures 4a and 4b are reproduced with the courtesy of C. Barth.)

1995 (close to solar minimum activity). The HUT UV spectrograph has a spectral range between 82 and 180 nm with a ∼0.4 nm spectral resolution. *Feldman et al.* [2000] concluded that the main source of the CO4P ($A^1\Pi$ - $X^1\Sigma^+$) band system is fluorescence of CO in both Venus and Mars upper atmospheres. In the spectrum of *Feldman et al.* [2000] of both Mars and Venus dayglows, the brightest feature in the spectral range 132 − 170 nm is at 165.7 nm. However, this discrepancy with SPICAM is most probably due to the much lower spectral resolution of SPICAM UVS. Moreover, spectra of Venus dayglow with 1.3 nm spectral resolution have been also measured by Pioneer Venus OUVS at high solar activity [*Durrance*, 1981] as well as from a rocket with a spectral resolution between 2.2 and 7 nm and for moderate solar activity [*Rottman and Moos*, 1973]. Both spectra displayed a brighter emission at 156.1 nm than at 165.7 nm.

[18] *Fox and Dalgarno* [1979] concluded from the measurement of the 165.7 nm emission in the Martian dayglow that resonant scattering of atomic carbon (^3P - $^3P^0$ multiplet emission) should be the main source of the observed emission at 165.7 nm (with an intensity up to
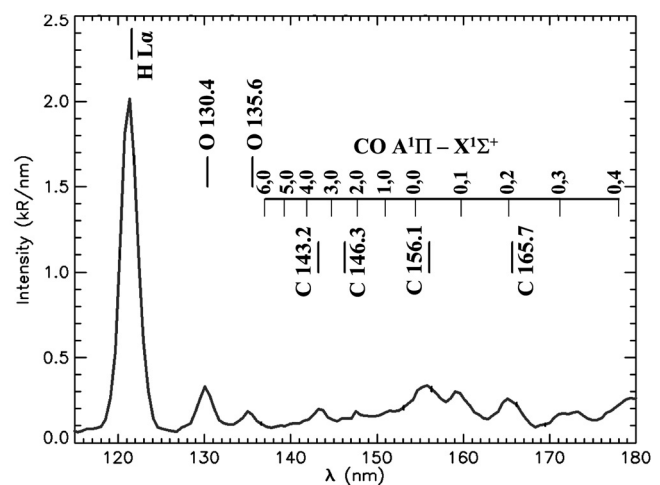
Figure 5. Spectrum obtained by SPICAM UV (the 100 − 180 nm spectral range) between SZA = 14 − 37° and Ls = 135 − 171° and between 140 − 150 km in altitude; 1224 individual spectra have been averaged. Most of the plotted error bars are smaller than the thickness of the line.

1.7 kR at 150 km in altitude [*Barth et al.*, 1971]). *Krasnopolsky* [1982] remade an earlier calculation by *McElroy and McConnell* [1971] and concluded that the main source of the 165.7 nm emission is instead related to the processes leading to the formation of atomic carbon (in particular dissociative excitation of CO_2 below 165 km). SPICAM UVS measured a maximum brightness for the emission at 165.7 nm equal to 900 Rayleigh at an altitude of 130 km for Ls = 135°–171° and equal to ∼500 Rayleigh at an altitude of 120 km at Ls = 100–135°. This measurement is therefore two to three times lower than the intensity considered by *Krasnopolsky* [1982] for high solar activity. This author calculated a maximum of 1.5×10^5 atoms of carbon per cm^3 at 155 km in order to reproduce Mariner 6 and 7 measurements. The measurement by SPICAM therefore suggests that the production of excited carbon atoms should be up to 3 times smaller at low solar activity than high solar activity and therefore that the carbon density at low solar activity might be up to 3 times smaller than at high solar activity. The atomic carbon density should be even lower since the 165.7 nm emission is contaminated by several fourth positive bands [*Paxton*, 1985], which was not taken into account in the calculation of *Krasnopolsky* [1982].

3. Analysis of SPICAM UVS Measurements

3.1. Thermosphere

[19] Figure 6 provides an example of the way that the Martian dayglow varies in altitude. Each spectrum displayed in Figure 6 has been obtained by averaging more than 1000 individual spectra measured during several different orbits. Only the H Lyman α emission does not vary significantly between 120 and 180 km in altitude, and in a lesser way, the O triplet at 130.4 nm. Both emissions are largely produced by resonant scattering of solar photons and are optically thick at line center. In contrast, the O doublet at 135.6 nm is a forbidden transition and excited primarily by electron impact on O or by dissociative excitation of CO_2 by electron impact (Table 1). This emission decreases significantly with respect to the resonant scattering emissions above 130 km in altitude, since the suprathermal electron flux is both expected [*Fox and Dalgarno*, 1979] and observed [*Bougher et al.*, 2004] to peak around 130 km.

[20] The emission of the CO Cameron band system, the emission of the CO_2^+ ultraviolet doublet ($B^2\Sigma^+$ - $X^2\Pi$) and the O emission at 297.2 nm all decrease with increasing altitude above 130 km. However, the ratio between these three emissions also changes with altitude. The emissions of the CO_2^+ ($B^2\Sigma^+$ - $X^2\Pi$) bands and the O 297.2 nm line decrease in intensity with respect to the intensity of Cameron band system. A simple decrease of the CO_2 atmospheric density would induce a proportional decrease of the intensity of all these emissions if these ones were produced essentially from CO_2 dissociative excitation. Actually, *Fox and Dalgarno* [1979] calculated that between the ionospheric peak and 200 km ∼15% of the emission of the Cameron band system is produced by dissociative recombination of CO_2^+. This estimate was based on density of CO_2^+ in the Martian ionosphere equal to of 5×10^3 cm^{-3} at 160 km and equal to 5×10^2 cm^{-3} at 200 km for low solar activity and a solar zenith angle of 45°. *Fox* [2004a] recently calculated for

a solar zenith angle of 60° at low solar activity a density of CO_2^+ at 160 km of ∼10^4 cm^{-3} and at 200 km of 10^3 cm^{-3} in good agreement with *Krasnopolsky* [2002]. Therefore, from the calculation of *Fox and Dalgarno* [1979] and these larger values for the CO_2^+ density, dissociative recombination of CO_2^+ could contribute up to 30% to the Cameron band emission. Since larger densities for CO_2^+ may be expected at lower solar zenith angle (up to 7×10^3 CO_2^+/cm^3 at 200 km and a solar zenith angle of 0° following *Ma et al.* [2004]), this contribution might be even larger than 30%. Moreover, since the scale height of the ionosphere is significantly larger than that of the neutral atmosphere (23 km scale height for the CO_2^+, from Viking 1 measurement [*Hanson et al.*, 1977]), the proportion of the CO Cameron band system emission due to dissociative recombination of CO_2^+ should increase with altitude. It should in particular result in a slower decrease of the CO Cameron band system emission with increasing altitude than emissions produced solely from dissociative or ionization excitation of CO_2. The distribution of the intensity between the bands of the CO Cameron band system also changes with altitude. Whereas the (0,1) band is the most intense emission below 160 km, the (1,0) band dominates the Cameron band system above, which is less consistent with a production of the CO Cameron band system by photon and electron dissociation of CO_2 [*Barth et al.*, 1971]. A peak at 276 nm is present in all the panels of Figure 6 (the origin of which is discussed section 3.2).

[21] Figure 7 displays the CO Cameron band system total intensity versus altitude measured by SPICAM for moderate solar activity (Table 2) compared to Mariner 6, 7 (high solar activity) and Mariner 9 (moderate solar activity) measurements. Part of the differences in intensity between SPICAM and Mariner 6 and 7 measurements are probably due to calibration. Indeed, *Stewart et al.* [1972] suggested that the factor of 2.5 between Mariner 9 measurements and Mariner 6 and 7 measurements (Figure 7) was due to both solar activity (reducing by 40% the Mariner 6 and 7 intensity) and also sensitivity overestimates in Mariner 6 and 7 cases (∼50%). In Figure 8, we plot the variation of the intensity of the CO_2^+ ($B^2\Sigma^+$ - $X^2\Pi$) emission versus altitude, using the same legend as for Figure 7. We did not find any data regarding this emission for the Mariner 9 UVS, but Mariner 6 and 7 profiles start significantly higher than the SPICAM-measured altitudes of the maximum of the intensity of this emission.

[22] There is a ratio of about 2 between the CO Cameron band system intensity as measured by SPICAM and the corrected measurements by Mariner 6, 7 and 9, as in the case of the CO_2^+ ($B^2\Sigma^+$ - $X^2\Pi$) ultraviolet doublet emission. A first potential explanation lies in solar activity. There is a clear dependence of the measured maximum of intensity of the CO Cameron band system emission with respect to solar activity (solar F10.7 index given Table 2). For solar zenith angle below 45°, the average maximum of intensity is equal to ∼164 kR for F10.7 between 80 and 100 (F10.7 average value equal to 89) and is equal to ∼195 kR for F10.7 index between 110 and 130 (F10.7 average value equal to 128). Mariner 9 observed during a period with a F10.7 index between 110 and 140, whereas the profiles displayed in Figures 7 and 8 have been obtained from the whole set of observations Table 2. Moreover, Mariner 9 observations
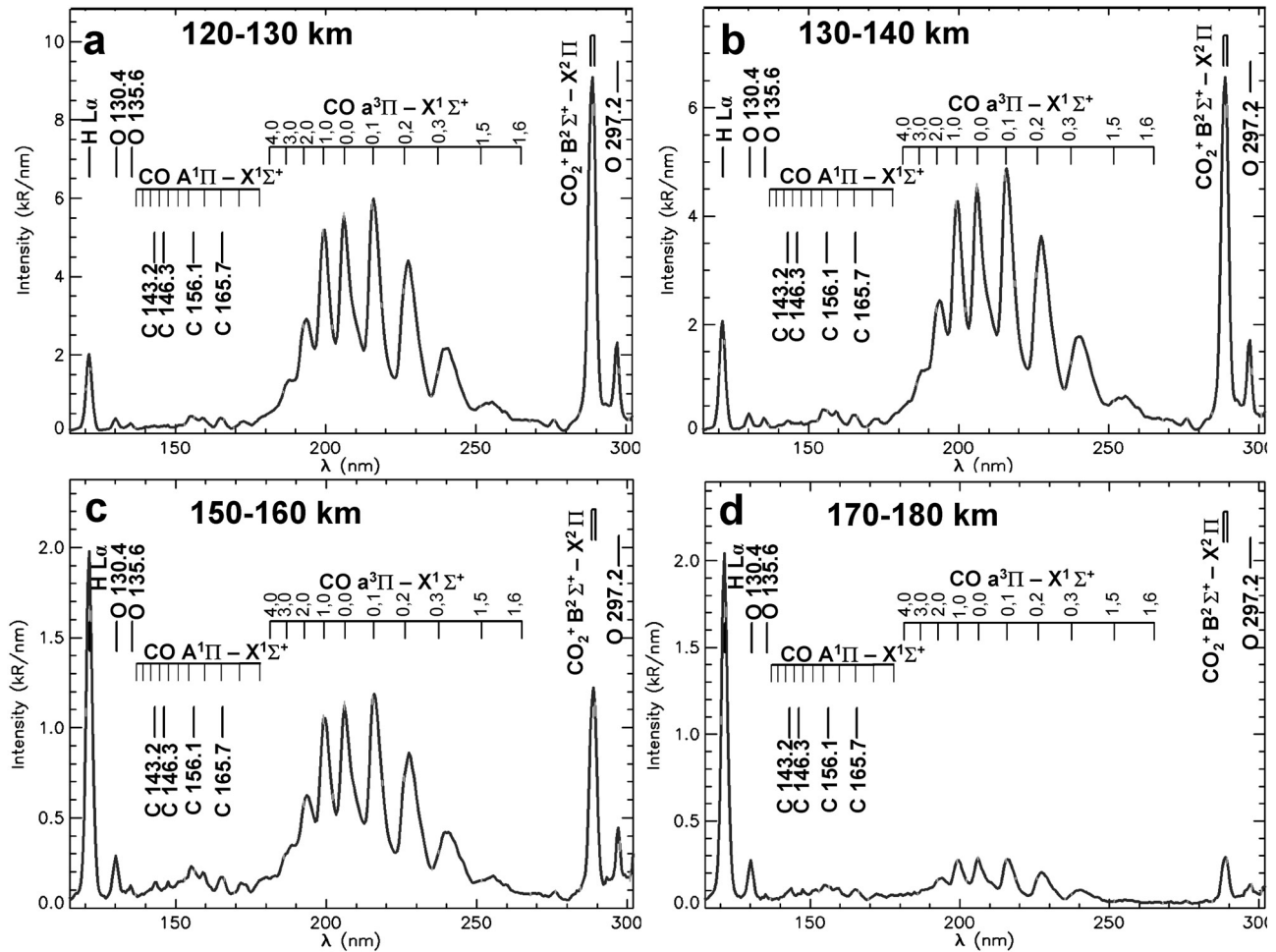
Figure 6. Spectra obtained by SPICAM UVS between SZA = 14 − 37° and Ls = 135 − 171°. (a) Average of 1102 individual spectra measured between 120 and 130 km. (b) Average of 1024 individual spectra obtained between 130 and 140 km. (c) Average of 1003 individual spectra obtained between 150 and 160 km. (d) Average of 1052 individual spectra obtained between 170 and 180 km. Most of the plotted error bars are smaller than the thickness of the line.

were done close to Mars' perihelion, whereas the present set of observations were obtained just after aphelion. The variation of Martian heliocentric distance equates to a difference of 1.4 in the intensity of the average solar flux at Mars and therefore of the expected dayglow brightness. Mariner 6 and 7 observations were done at Ls = 200°, that is, only slightly closer to the Sun than the SPICAM observations. However, they were also done during high solar activity with a F10.7 index between 167 and 188. Another source of variation of these emission intensities is a solar zenith angle dependence. As displayed in Figures 7 and 8, in going from solar zenith angles between 14° and 37° to solar zenith angles between 60° and 83°, the intensities of the CO Cameron band system emission and the CO_2^+ ($B^2\Sigma^+$ - $X^2\Pi$) doublet emission decrease significantly in brightness (see also Figure 12). Mariner 9 profiles were obtained at solar zenith angle between 7 and 23°, whereas Mariner 6 and 7 measurements were obtained at 27° and 44° solar zenith angle, respectively. Therefore the largest sources of variation of the CO Cameron band system

and the CO_2^+ ($B^2\Sigma^+$ - $X^2\Pi$) ultraviolet doublet emissions are related to the solar activity and to the solar zenith angle and may explain the differences with Mariner 6, 7 and 9 observations.

[23] The altitude of the maximum dayglow intensity is around 130 km in the Mariner observations, whereas it is significantly lower in SPICAM measurements at Ls < 130.1° (Figure 7a). For the Mariner 9 observations reported by *Stewart et al.* [1972], this difference could result from a planetwide dust storm which heated the lower atmosphere and raised the altitude of the thermosphere. Moreover, as displayed in Figures 7 and 8, the altitude of the maximum observed by SPICAM increases significantly with aerocentric longitude: moving from 112.5 km and 117.5 km for the CO_2^+ ($B^2\Sigma^+$ - $X^2\Pi$) ultraviolet doublet emission and the CO Cameron band system, respectively, for Ls < 130.1° (Figures 7a and 8a) up to 122.5−132.5 km for the same emissions at Ls > 138° (Figures 7b and 8b). The later (Ls > 138°) altitudes for the maximum emission of the CO Cameron band system observed by SPICAM are in good agreement
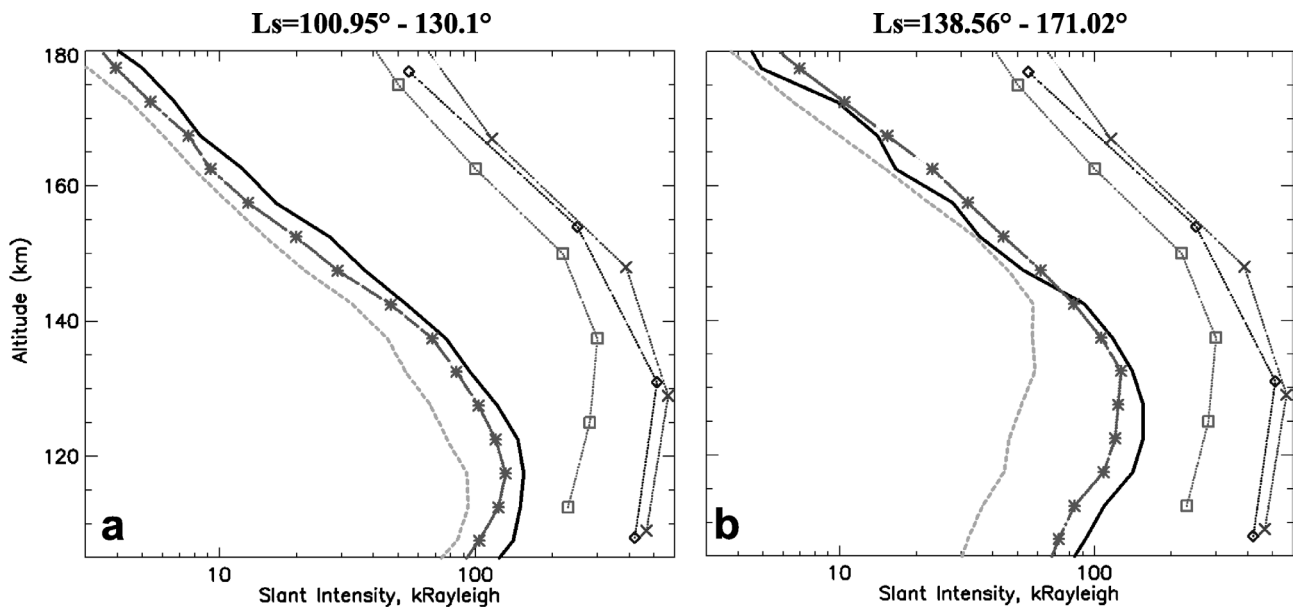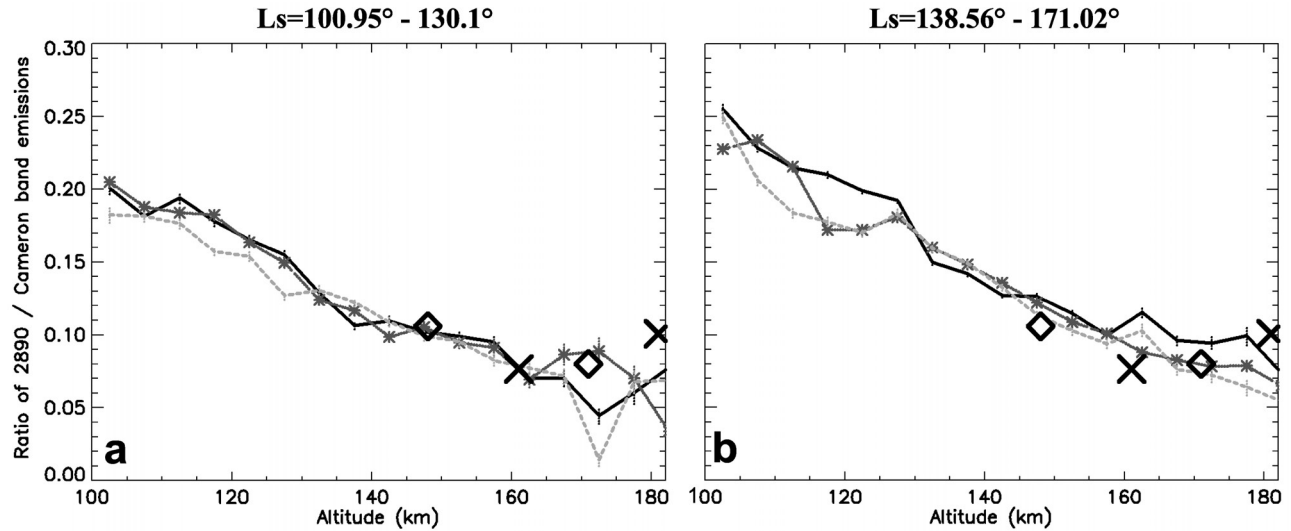
Figure 7. Variation of the CO Cameron band intensity versus altitude (with 4-km altitude resolution) between 190 and 270 nm. (a) Ls = $100.95°$ − $130.1°$ with 10 orbits. (b) Ls = $138.56°$ − $171.02°$ with 14 orbits. Dotted cross line: Mariner 7, one limb observation at Ls = $200°$ and SZA = $44°$ [*Barth et al.*, 1971]. Dotted diamond line: Mariner 6, one limb observation at Ls = $200°$ and SZA = $27°$ [*Barth et al.*, 1971]. Dotted square line: Mariner 9, one limb observation taken between SZA = $7°$ and $23°$ at Ls = $312°$ [*Stewart et al.*, 1972]. Thick dark line: SPICAM between SZA = $15°$ and $37°$. Star dashed line: SPICAM between SZA = $37°$ and $60°$. Gray dashed line between SZA = $60°$ and $83°$.

with those reported by Mariner 6 and 7, as well as with radio occultation measurements done at SZA~$80°$ [*Bougher et al.*, 2004]. This apparent variation of the altitude of the maximum intensity of the CO Cameron

band system emission cannot be explained by differences in the conditions of the observations between the orbits at Ls < $130.1°$ and those at Ls > $138°$. This is particularly true for the observations at low solar zenith angle since
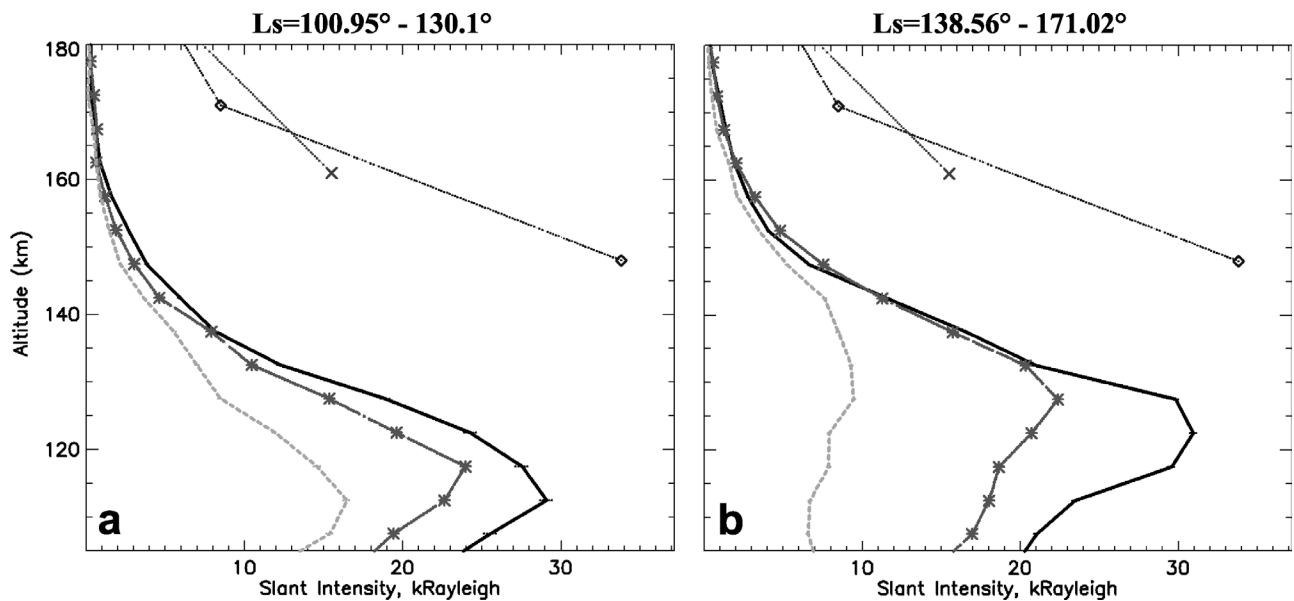
Figure 8. Variation of the CO_2^+ ($B^2\Sigma^+$ - $X^2\Pi$) ultraviolet doublet intensity versus altitude (with 4-km altitude resolution). (a) Ls = $100.95°$ − $130.1°$ with 10 orbits. (b) Ls = $138.56°$ − $171.02°$ with 14 orbits. Dotted cross line: Mariner 7, one limb observation at Ls = $200°$ and SZA = $44°$ [*Barth et al.*, 1971]. Dotted diamond line: Mariner 6, one limb observation at Ls = $200°$ and SZA = $27°$ [*Barth et al.*, 1971]. Thick dark line: SPICAM between SZA = $15°$ and $37°$. Star dashed line: SPICAM between SZA = $37°$ and $60°$. Gray dashed line between SZA = $60°$ and $83°$.

Figure 9. Variation of the intensity ratio between the CO Cameron band and the CO_2^+ ($B^2\Sigma^+ - X^2\Pi$) doublet as a function of altitude (with 4-km altitude resolution). (a) Ls = $100.95° - 130.1°$ with 10 orbits. (b) Ls = $138.56° - 171.02°$ with 14 orbits. Thick dark line: SPICAM between SZA = 15° and 37°. Star dashed line: SPICAM between SZA = 37° and 60°. Gray dashed line between SZA = 60° and 83°. Diamonds: intensity ratio as deduced from the measurements done at SZA = 27° and Ls = 200° by Mariner 6. Crosses: intensity ratio deduced from the measurements done at SZA = 44° and Ls = 200° by Mariner 7.

for both periods of the Martian year, the low solar zenith angle observations have been done close to the equator in Mars early afternoon.

[24] *Stewart et al.* [1972] suggested a solar activity dependence of the subsolar zenith intensity of the total CO Cameron band system as I(kR) = 0.062 × (74 + F10.7). The maximum value of the Cameron band system intensity observed by SPICAM with limb viewing is ∼150 kR for $14°-37°$ solar zenith angle. The zenith or overhead emission can be estimated from an optically thin limb viewing intensity by dividing by the ratio of path lengths toward the limb and toward the zenith, $L_{limb}/L_{zenith} \sim (2\pi \times R_M/Hs)^{1/2}$, where R_M is Mars' radius and Hs is the scale height of the CO_2 near the emission peak, which is here observed to be between 12 and 14 km. Thus the ∼165 kR subsolar limb viewing intensity corresponds to a zenith subsolar intensity of 4 kR. F10.7 during the SPICAM observations was between 80 and 130 (Table 2). Following *Stewart et al.* [1972], the predicted intensity for the zenith subsolar CO Cameron band emission should be between 9.5 and 12.6 kR, significantly above our present measurements.

[25] *Stewart et al.* [1972] analyzed several profiles of the CO Cameron band system and CO_2^+ ($B^2\Sigma^+ - X^2\Pi$) ultraviolet doublet emissions and concluded that in the Martian upper atmosphere (above ∼140 km in altitude) both emissions are essentially produced by photoexcitation of CO_2. These authors also indicated that the average value of the ratio of these two emission intensities is equal to 0.24. In Figure 9, the ratio of the intensities of the CO_2^+ ($B^2\Sigma^+ - X^2\Pi$) doublet emission to the CO Cameron band system significantly decreases with altitude from a value at 110 km of ∼0.2 at Ls < 138° and ∼0.25 at Ls > 138° down to values at 170 km ∼0.08 and ∼0.1 for Ls < 138° and Ls > 138°, respectively.

Mean values are significantly larger than the earlier estimate by *Stewart et al.* [1972]. Actually, one of the differences in our observations of the Martian dayglow between these two periods of aerocentric longitude is the altitude of the peak of the maximum emission intensity, which moves ∼10 km higher at higher Ls values. If the altitude scale of Figure 9a is changed by 10 km, we retrieve the profile of Figure 9b. No dependence of this ratio versus SZA is evident in Figure 9. We also plotted in Figure 9 the values of this ratio deduced from the measurements done by Mariner 6 and 7 [*Barth et al.*, 1971]. The very good agreement between these values and the ones we deduced from SPICAM observations suggests therefore that this ratio is only weakly dependent on the solar activity.

[26] As shown in Table 1, the CO ($a^3\Pi - X^1\Sigma^+$) Cameron band system emission is essentially produced by electron or photon dissociative excitation of the CO_2 molecule, by dissociative recombination of CO_2^+ (significantly more than 15% following our previous discussion), and in negligible way by direct photon or electron excitation of the CO molecule. The CO_2^+ ($B^2\Sigma^+ - X^2\Pi$) ultraviolet doublet emission is produced by photon and electron ionization and excitation of the CO_2 molecule [*Fox and Dalgarno*, 1979; *Fox*, 1992]. A minor part of this latter emission may be also produced by CO_2^+ fluorescent emission [*Stewart*, 1972; *Hanson et al.*, 1977], but less than 4% according to *Fox and Dalgarno* [1979]. This may be doubled following the most recent estimates of the CO_2^+ density above the ionospheric peak [*Krasnopolsky*, 2002; *Fox*, 2004a; *Ma et al.*, 2004]. The observed faster decrease above the ionospheric peak of the CO_2^+ ($B^2\Sigma^+ - X^2\Pi$) doublet emission relative to the CO Cameron band system emission may be therefore explained by an increase of the contribution of the

CO_2^+ dissociative recombination excitation to the CO Cameron band system emission.

[27]   The exospheric temperature between 150 km and 200 km in altitude can be retrieved by a simple analysis of the CO Cameron band system and CO_2^+ $(B^2\Sigma^+ - X^2\Pi)$ doublet profiles by supposing that within this altitude range the atmosphere can reasonably be considered to be close to a barometric isotherm atmosphere, optically thin, and that the main process leading to these two emissions is photo-dissociative excitation of CO_2 for the CO Cameron band system and photo-ionization of CO_2 for the CO_2^+ $(B^2\Sigma^+ - X^2\Pi)$ doublet emission in this region of the upper atmosphere [Fox and Dalgarno, 1979]. Such a method has been used to analyze Mariner 6 and 7 data by Stewart [1972], who deduced a scale height for the upper atmosphere Cameron band system equal to 19±4.5 km, corresponding to a temperature of 315±75 K. A similar analysis of the CO_2^+ $(B^2\Sigma^+ - X^2\Pi)$ doublet resulted in a best estimate for this temperature of 350 K. The same analysis from 18 different profiles of Cameron band emissions measured by Mariner 9 yielded scale heights of between 14.8 and 24.3 km (mean 17.8 km), implying a temperature between 270 and 445 K with a mean of 325 K [Stewart et al., 1972].

[28]   As shown in Figure 9, the ratio of the CO Cameron band system and the CO_2^+ $(B^2\Sigma^+ - X^2\Pi)$ doublet emissions changes as a function of altitude from 130–170 km, by up to 50%. In order to define the best altitude range to calculate a representative scale height of the atmosphere, we estimated the altitude above which this ratio was approximately constant (any remaining variation of this ratio at higher altitudes being <1σ from the mean value). We then calculated the scale height of both emissions from this altitude up to a range of altitude between 170 km and 190 km. The results of this calculation from the Cameron band system emission are as follows:

[29]   1. T~267 K (scale height = 14.2 km) at Ls = [100°, 138°] and T~257 K (scale height = 14.3 km) at Ls = [138°, 171°] for SZA = 14°–37° (black solid lines, Figure 7).

[30]   2. T~243 K (scale height = 12.6 km) at Ls = [100°, 138°] and T~257 K (scale height = 14.3 km) at Ls = [138°, 171°] for SZA = 37°–60° (gray solid lines with stars, Figure 7).

[31]   3. T~257 K (scale height = 14.3 km) at Ls = [100°, 138°] and T~228 K (scale height = 12.7 km) at Ls = [138°, 171°] for SZA = 60°–83° (dashed gray lines, Figure 7).

[32]   The same analysis for the CO_2^+ $(B^2\Sigma^+ - X^2\Pi)$ ultraviolet doublet emission leads to significantly lower temperatures:

[33]   1. T~198 K (scale height = 10.5 km) and T~219 K (scale height = 12.2 km) at Ls = [100°, 138°] and Ls = [138°, 171°] for SZA = 14°–37° (black solid lines, Figure 8).

[34]   2. T~202 K (scale height = 10.6 km) and T~207 K (scale height = 11.5 km) at Ls = [100°, 138°] and Ls = [138°, 171°] for SZA = 37°–60° (gray solid lines with stars, Figure 8).

[35]   3. T~191 K (scale height = 10.6 km) and T~191 K (scale height = 10.6 km) at Ls = [100°, 138°] and Ls = [138°, 171°] for SZA = 60° – 83° (gray dashed lines, Figure 8).

[36]   The mean value of the temperature is equal to 252 ± 13 K when calculated from the CO Cameron band system emission and equal to 201 ± 10 K when calculated from the CO_2^+ $(B^2\Sigma^+ - X^2\Pi)$ doublet emission. There is no evident dependence of these temperatures on SZA (see also Figure 10) or Ls (see the end of this section for further discussion). More interestingly, there is an obvious systematic lower scale height associated with the CO_2^+ $(B^2\Sigma^+ - X^2\Pi)$ doublet (~11.2 km) than the scale height associated with the CO Cameron band system (~14 km). As discussed previously, the Cameron band emission might be produced in a significant proportion by dissociative recombination of CO_2^+ in particular above the ionospheric peak. On the other hand, the contribution of the CO_2^+ fluorescent scattering to the CO_2^+ $(B^2\Sigma^+ - X^2\Pi)$ ultraviolet doublet emission should remain smaller than 10%. Therefore the scale heights deduced from the CO_2^+ $(B^2\Sigma^+ - X^2\Pi)$ ultraviolet doublet are probably closer to the neutral atmospheric scale heights than the scale heights deduced from the Cameron band emission. The range of temperature we found by this analysis is in agreement with MGS accelerometer experiment results of between 220 and 230 K (during a Full Martian year) and with the Martian Thermospheric Global Circulation Model which predicts solar minimum temperatures of 200 and 220 K between aphelion and perihelion [Bougher et al., 2000]. Viking 1 and 2 descent probes at low solar activity, Ls ~100° and SZA~41° also derived temperatures below 200 K, which are not far from the values we derived from the profile of the emission intensity of the CO_2^+ $(B^2\Sigma^+ - X^2\Pi)$ ultraviolet doublet.

[37]   We also performed the same analysis of these emissions for each individual orbit. The results of this analysis are given in Table 2 for the CO Cameron band system and CO_2^+ $(B^2\Sigma^+ - X^2\Pi)$ doublet emissions. On average, T~246 K with a standard deviation equal to 47 K when deduced from the CO Cameron bands and T~191 K with a standard deviation equal to 46 K when deduced from the CO_2^+ $(B^2\Sigma^+ - X^2\Pi)$ doublet emission. The scale height of the Cameron band varies between 10.6 and 20.5 km. As noted above, we do not observe any systematic trends of the derived temperatures with SZA, aerocentric longitude Ls, longitude (i.e., no apparent atmospheric tide effect) or latitude.

[38]   We also display in Table 2 (also Figure 11) the altitude of the peak intensity of the CO Cameron band observed during each orbit (therefore, for most of the cases, two values, one for downleg and one for upleg). The peak altitude varies with solar zenith angle, moving from 120 km at SZA~30° up to 132 km at SZA~75° (in good agreement with radio occultation measurements [e.g., Bougher et al., 2004]). Likewise, we observed a dependence of the peak altitude with aerocentric longitude, the average peak altitude being ~115 km for Ls = [100°, 138°] and ~130 km for Ls = [138°, 171°] (Figure 11c). Chapman layer theory predicts a variation of the peak altitude versus SZA following a law in H × ln(sec(SZA)) [Hantsch and Bauer, 1990] where H is the scale height of the atmosphere (between 11.2 and 14 km according to this present analysis) and SZA is the local solar zenith angle. We did not find any apparent relation of this type which may be due to the small available sample (Figure 11a). No dependence of the altitude of this peak is found versus longitude (Figure 11b, even when binned in different solar zenith angle ranges), solar zenith angle or latitude. The rather small size of our present sample (only 45 points distributed in longitude) may explain this lack of
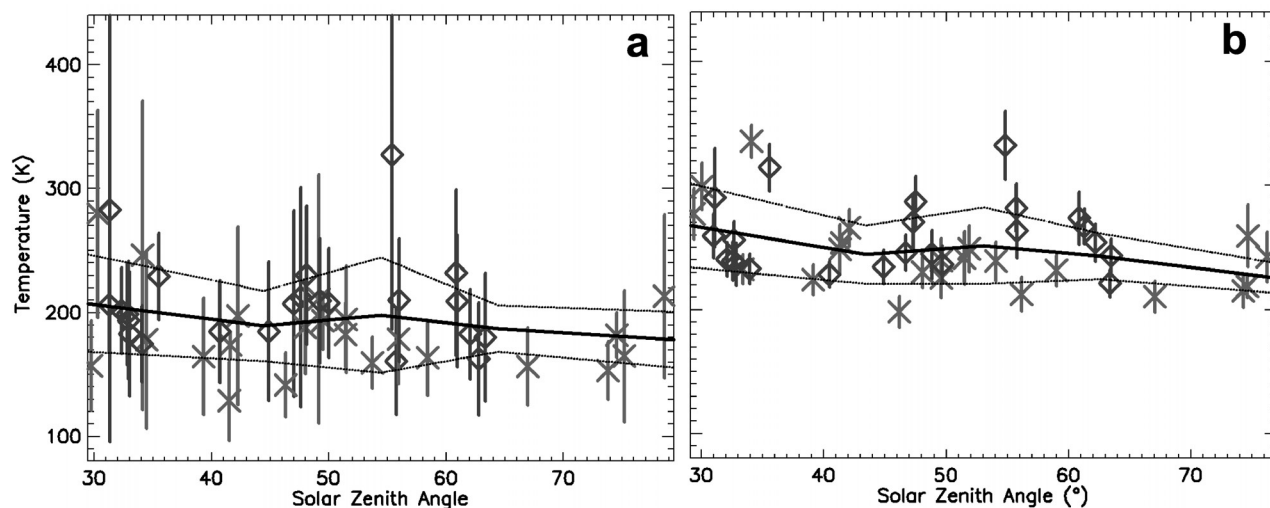
Figure 10. Variation of the temperatures versus SZA (Table 2). Crosses and diamonds are for downleg and upleg of the orbit, respectively. The vertical bar represents the maximum and minimum value of the temperature retrieved using the method described in section 3.1. The solid line represents the mean temperature, and the two dotted lines represent the mean temperature plus or minus one standard deviation. (a) As deduced from CO_2^+ ($B^2\Sigma^+$ - $X^2\Pi$) ultraviolet doublet intensity. (b) As deduced from the CO Cameron band intensity.

observation of any migrating wave effect [*Bougher et al.*, 2004]. The last column of Table 2 provides the maximum intensity of the Cameron band emission for each of the analyzed orbits. The only significant variation of this maximum intensity is with respect to SZA (Figure 12), with a peak intensity decreasing from roughly 200 kR at SZA = 30° down to 50 kR at SZA = 75°. This intensity variation should follow a $\cos^{1/2}$(SZA) dependence according to Chapman layer theory [*Hantsch and Bauer*, 1990; *Breus et al.*, 2004]. Again, we failed to find any variation following such a law (even excluding measurements made during high solar activity). Actually a cos(SZA) law provides the best fit.

### 3.2. Potential Explanation for the 276 nm Feature in the SPICAM Spectra

[39] As noted in the previous section, a significant feature is apparent in most of the spectra recorded by SPICAM around 276 nm. It is interesting that this feature was also observed in the spectrum of the auroral event reported by *Bertaux et al.* [2005b]. A possible explanation for this feature is illustrated in Figure 13, which displays the average of 2970 individual spectra taken during more than 10 different orbits. As shown in this figure, we tentatively identify this feature as the (0,6) band of the N_2 Vegard-Kaplan ($A^3\Sigma^+$ - $X^1\Sigma^+$) band system which is at 276.2 nm. Actually, other bands may also be present in the Figure 13 spectrum, but with small S/N ratio, e.g., the (0,7) band at 293.6 nm and the (0,5) band at 260.4 nm. In Mariner 9 spectra (Figure 4a), a feature at 293.6 nm is also visible and actually more distinct from the two much brighter emissions at 289 nm and 297.2 nm than in the SPICAM spectrum (Figure 13).

[40] *Fox et al.* [1977] and *Fox and Dalgarno* [1979] predicted that the (0,5), (0,6) and (0,7) bands should correspond to the most intense emissions within the Vegard-Kaplan band system, and they are expected to be the most intense features associated with N_2 emission within the spectral range of SPICAM. The Vegard-Kaplan bands have been described by these authors as produced by electron impact excitation on N_2 and associated with an overhead intensity of ~20 Rayleighs for the (0,6) and (0,7) bands and ~16 Rayleighs for the (0,5) band. Other bands exist at 313.2 nm (14 Rayleighs for band (0,8)), at 299.8 nm (10 Rayleighs for band (1,8)) and at 319.9 nm (15 Rayleighs for band (1,9)). However, these four bands are either at the limit of the sensitivity of SPICAM or else are overlapped by other, more intense emissions.

[41] The intensity of a limb viewing emission can be estimated from the zenith intensity by scaling by the ratio of path lengths $L_{limb}/L_{zenith} \sim (2\pi \times R_M/Hs)^{1/2}$ where R_M is Mars' radius and Hs is the scale height of N_2. Since we find the typical scale height for CO_2 in Mars' thermosphere is between 11.2 and 14 km, the N_2 scale height should be between 19 and 22 km. Therefore the ratio of path lengths is ~30, which implies that the overhead intensities calculated by *Fox and Dalgarno* [1979] correspond to limb viewing peak brightnesses of 600 Rayleigh for the (0,6) and (0,7) bands and 480 Rayleigh for the (0,5) band.

[42] Figure 14 displays the profiles of the SPICAM-measured intensities for the three features at 260.4 nm, 276.2 nm and 293.6 nm. The maximum observed values for these intensities are ~300 Rayleighs for the 276.2 nm (0,6) band, 110 Rayleighs for the 260.4 nm (0,5) band and ~40 Rayleighs for the 293.6 (0,7) band. For this latter band, the emission is unfortunately sandwiched between two much more intense emissions at 289 nm and 297.2 nm. This band therefore has a large uncertainty when extracted from SPICAM spectrum by the direct integration method (Appendix A, section A2). Our estimates for the intensity of these three bands, in particular of the (0,6) band, are in surprisingly good agreement (only two times less intense) with the *Fox and Dalgarno* [1979] predictions, despite the fact that we used a very simple method to extract these
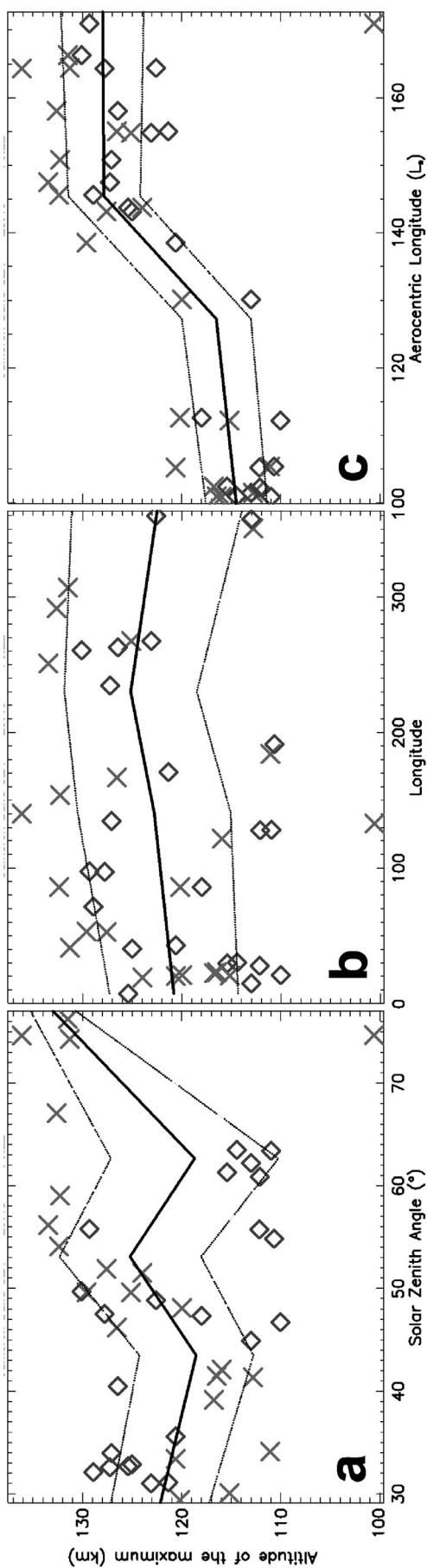
intensities. Moreover, *Fox and Dalgarno* [1979] neutral model at low solar activity predicted mixing ratios of N_2/CO_2 between 8 and 15% at 140 and 160 km in altitude, which has been more recently estimated to be less than 10% [*Fox*, 2004b; *Krasnopolsky*, 2002].

[43] The variation with altitude of the intensity of these three features behaves like typical electron impact generated dayglow emissions, with a peak around 115 – 140 km and a quick decrease above 140 km in altitude (Figure 14). The maximum intensity is reached slightly above the peak of the CO Cameron band emission, in good agreement with the prediction of *Fox et al.* [1977] when considering the quenching of the $A^3\Sigma^+$ excited state with CO_2 molecules [*Dalgarno and McElroy*, 1970]. Such a dependence with altitude rules out any possibility that the features are due to stray light, and confirms that they are real dayglow emissions.

[44] Although we favor the N_2 Vegard-Kaplan band explanation, other possibilities exist for the feature at 276 nm, even though we consider them less probable. For example, it could correspond to the O_2 Herzberg I (6,2) band emission resulting from O+O recombination [*Eastes et al.*, 1992], similar to NO recombination emission [*Bertaux et al.*, 2005a]. Another possibility is an emission associated with CO^+ excitation by electron impact ionization/excitation of CO molecules [*Cossart and Cossart-Magos*, 1996].

3.3. Exosphere

[45] Above 180 km in altitude, the dayglow is dominated by Lyman α emission, associated with resonant scattering of sunlight by H atoms in the Martian exosphere. Above 200 km, the second most intense emission is the 130.4 nm triplet of O, which is predicted to be the dominant species from 200–400 km during solar minimum activity [*Krasnopolsky*, 2002].

[46] Figure 15 displays the intensity of the Lyman α emission from 105 km up to 400 km in altitude. This figure also indicates the dependence of this emission versus SZA (roughly following a $\cos^{1/2}$(SZA) law). In Figure 15, we have not subtracted the interplanetary Lyman α emission estimated to contribute $\sim$0.3 kR in the case of Mariner 6 and 7 observations [*Barth et al.*, 1971]. A comparison between Figures 15a and 15b also suggests a significant variation of the Lyman α emission with respect to aerocentric longitude (essentially due to variation of the distance to the Sun). The maximum intensity is in good agreement with the measurement of *Barth et al.* [1971], who reported close to the planet an intensity for the Martian exospheric Lyman α emission equal to 4−5 kR as observed by Mariner 6 for SZA = 0° and 27° and to 3−4 kR as observed by Mariner 7 for SZA = 0° and 44° (with a 300 Rayleigh Lyman α sky background contribution subtracted). These measurements were measured during solar maximum activity, whereas a measurement of 3.3 kR ± 0.8 kR intensity for the Martian exospheric Lyman α emission was obtained
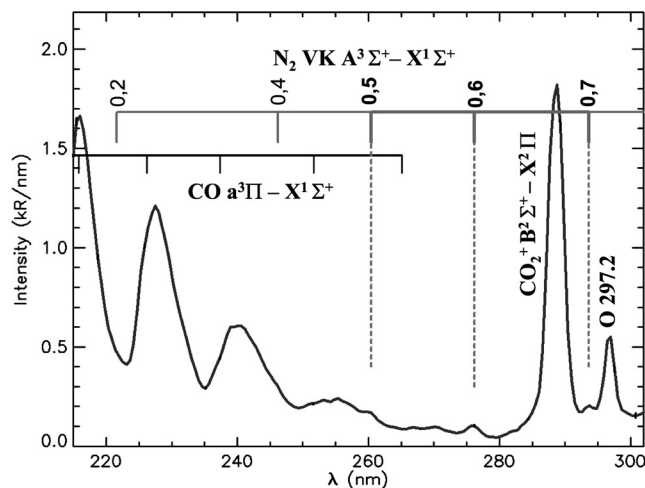

Figure 11. Altitude of the maximum of the Cameron band emission intensity (Table 2). (a) Versus solar zenith angle. (b) Versus longitude. (c) Versus aerocentric longitude. Crosses and diamonds are for downleg and upleg of the orbit, respectively. The solid line represents the mean altitude, and the two dotted lines represent the mean altitude plus or minus one standard deviation.
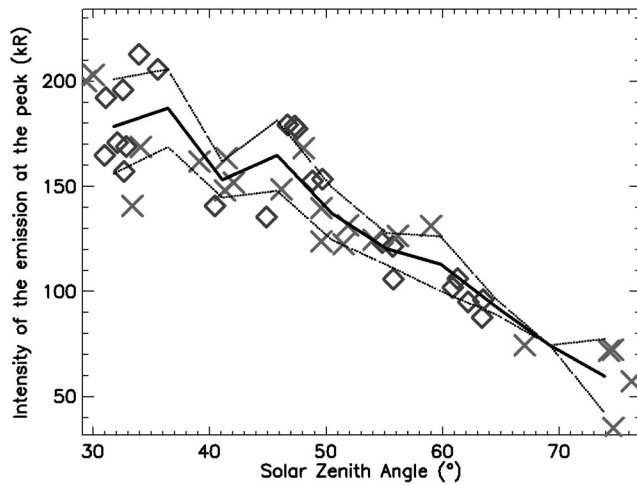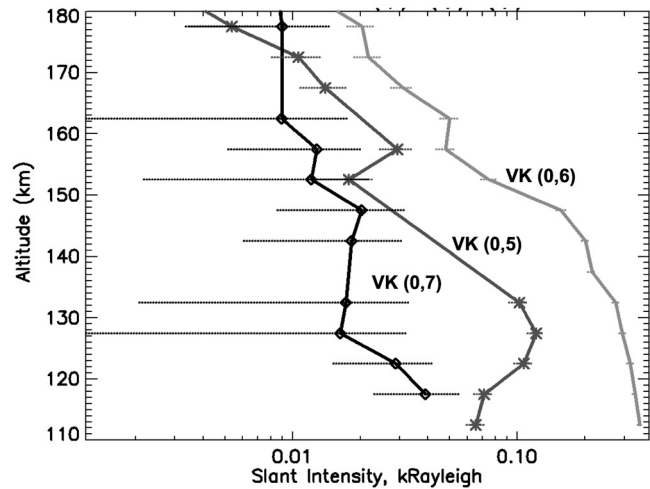
Figure 12. Maximum measured intensity of the Cameron band emissions (Table 2). Crosses and diamonds are for downleg and upleg of the orbit, respectively. The solid line represents the mean intensity, and the two dotted lines represent the mean intensity plus or minus one standard deviation.
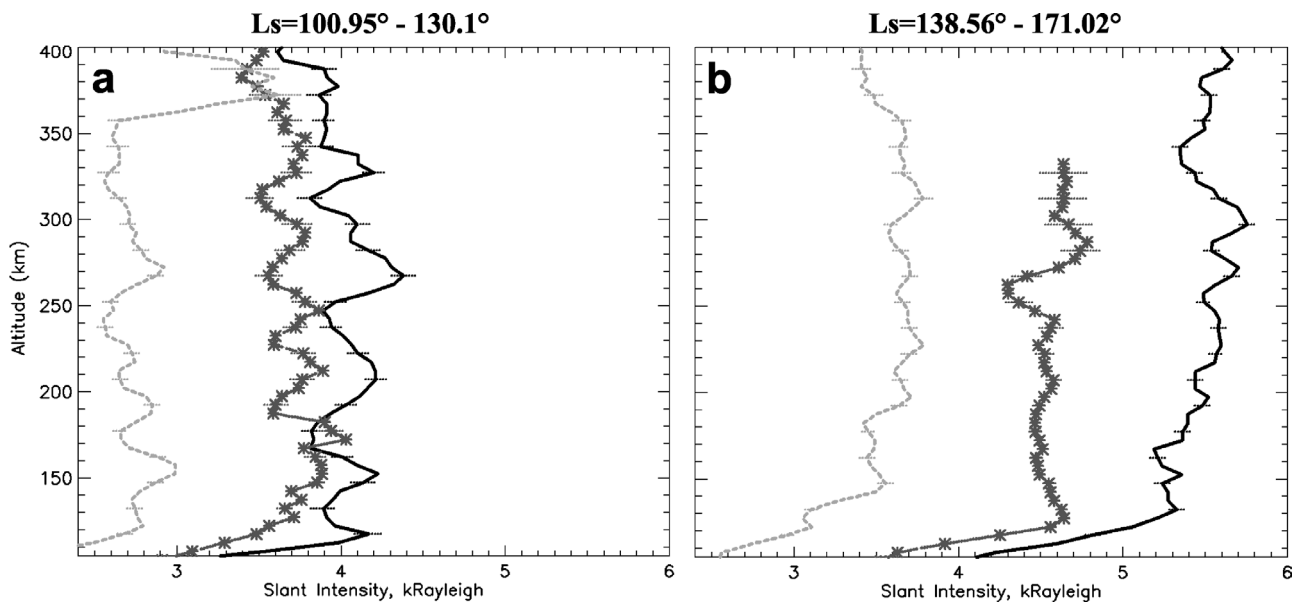

Figure 14. Variation of the intensity versus altitude (with 4-km altitude resolution) of the 260.4 nm emission feature, the (0,5) Vegard-Kaplan band (solid gray line with star), the 276 nm emission feature, the (0,6) Vegard-Kaplan band (solid gray line), and the 293.6 nm emission feature, the (0,7) Vegard-Kaplan band (solid dark line with diamond) for the entire set of observations described in this paper.

using the Copernicus Orbiting Astronomical Observatory [*Levine et al.*, 1978] during solar minimum activity.

[47] In Figure 16, we plot the oxygen emission at 130.4 nm measured by SPICAM between 120 and 400 km in altitude. The 130.4 nm emission is thought to be primarily produced by resonant scattering of sunlight by O atoms. *Strickland et al.* [1973] suggested that below 200 km one fourth of the observed intensity may be due to dissociative excitation of CO_2. Figure 16 clearly shows that the 130.4 nm dayglow emissions during SPICAM observations were significantly

less bright than during Mariner 6 (diamond black dotted line), Mariner 7 (cross dotted line) and Mariner 9 (square dotted line). Figure 16 also indicates a more significant dependency of the 130.4 nm emission on SZA than on aerocentric longitude. *Strickland et al.* [1973] observed that the Mariner 7 observations of this emission were 20 to 30% lower in intensity than observed by Mariner 9 and attributed these differences to a calibration error in the Mariner 6 and 7 UV spectrometers, as already discussed, or to a larger solar flux during Mariner 9 observations. According to these authors, a 20 to 30% lower intensity for the 130.4 nm emission implies an oxygen density smaller by around one order of magnitude (because the 130.4 nm emission is optically thick). Therefore, in order to explain the observed variations of the oxygen emission with respect to SZA, the density of oxygen within Mars' atmosphere should decrease by one order of magnitude from a solar zenith angle between $14 - 37°$ to a solar zenith angle of $37 - 60°$. There is also a significant increase of the scale height of the oxygen 130.4 nm emission with larger SZA which can be explained either by the decrease of the optical thickness or by the increase of the proportion of nonthermal oxygen atoms with increasing SZA.

[48] All these elements will be analyzed in a future paper using a 3D model of the hydrogen and oxygen upper atmosphere and exosphere combined with a resonance line radiative transfer analysis which accounts for the scattering optical thickness of these two emissions, as well as absorption by CO_2.

3.4. Martian Crustal Magnetic Field Influences on the Upper Atmosphere Structure

[49] Table 2 indicates a large increase during Orbit 983 of the upper atmosphere temperatures deduced from the CO Cameron band system and the CO_2^+ ($B^2\Sigma^+$ - $X^2\Pi$) doublet

Figure 13. Spectrum of the Martian dayglow between 145 and 150 km in altitude, averaged from 2970 individual spectra measured by SPICAM (i.e., the whole set of observations described in this paper). The solar zenith angle range is between $14°$ and $105°$, and the aerocentric longitude range is between $100.95°$ and $171.2°$. Most of the plotted error bars are smaller than the thickness of the line.

Ls=100.95° - 130.1°   **Ls=138.56° - 171.02°**
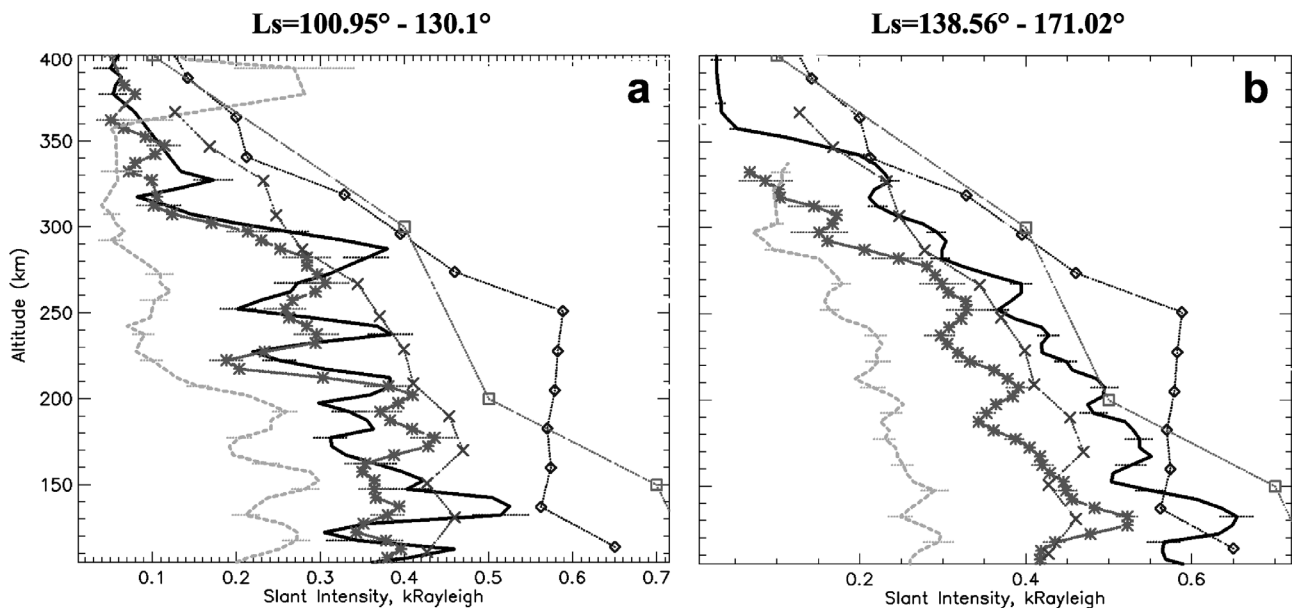

Figure 15. Variation of Lyman α intensity versus altitude (with 4-km altitude resolution). (a) Ls = 100.95° − 130.1° with 10 orbits. (b) Ls = 138.56° − 171.02° with 14 orbits. Thick dark line: SPICAM between SZA = 15° and 37°. Star dashed line: SPICAM between SZA = 37° and 60°. Gray dashed line between SZA = 60° and 83°.

emissions. As mentioned in section 2.2, orbit 983 is the only orbit during which the SPICAM FOV passed above the strongest crustal magnetic field structure (Figure 3). The crustal field is now recognized as inducing significant changes in the Martian upper atmosphere/ionosphere [*Krymskii et al.*, 2002; *Breus et al.*, 2004], as well as being related to aurora phenomena at Mars [*Bertaux et al.*, 2005b].

[50] The temperatures determined during orbit 983 are 336 K and 246 K (from the CO Cameron band system and

Ls=100.95° - 130.1°   **Ls=138.56° - 171.02°**

Figure 16. Variations of the OI 130.4 nm intensity versus altitude (with 4-km altitude resolution). (a) Ls = 100.95° − 130.1° with 10 orbits. (b) Ls = 138.56° − 171.02° with 14 orbits. Dotted cross line: Mariner 7, one limb observation at Ls = 200° and SZA = 44° [*Barth et al.*, 1971]. Dotted diamond line: Mariner 6, one limb observation at Ls = 200° and SZA = 27° [*Barth et al.*, 1971]. Dotted square line: Mariner 9 SZA = 31 − 36° [*Strickland et al.*, 1973]. Thick dark line: SPICAM between SZA = 15° and 37°. Star dashed line: SPICAM between SZA = 37° and 60°. Gray dashed line between SZA = 60° and 83°.

CO_2^+ ($B^2\Sigma^+$ - $X^2\Pi$) ultraviolet doublet emissions, respectively) during the period when the FOV was passing through region between 20°N and 16°N latitudes (at an almost constant longitude of 180°), and 332 K and 328 K between 16°S and 21°S latitudes (at an almost constant longitude of 190°). These temperature values are greater by 1–3 standard deviation values than the average corresponding temperatures. The altitude of the maximum intensity of the Cameron band system emission is slightly below the average one, but not significantly so. The peak brightness does not display any significant difference with respect to the average value.

[51] During this period, no apparent increase of the visible atmospheric opacity was observed (P. Rannou, personal communication, 2006). This was checked, since dust storms have been observed to increase the altitude of the electron density peak [*Keating et al.*, 1998] and, as suggested by *Stewart et al.* [1972], to potentially affect the upper atmosphere temperature [*Bougher et al.*, 2000]. Actually, what we observed during orbit 983 was, to the contrary, a slight decrease of the altitude of the peak of intensity of the CO Cameron band system emission. Moreover, orbit 981 which occurred 15 hours earlier than orbit 983, does not display any increase of either the peak altitude or the temperature. Atmospheric tides have been studied using MGS radio occultation and accelerometer measurements [*Keating et al.*, 2003; *Bougher et al.*, 2004]. In particular, *Bougher et al.* [2004] reported strong wave number 2–3 oscillations in electron density peak heights as a function of longitude. No influence of these atmospheric tides on the upper atmosphere temperature has been reported. A short time variation of solar activity (by less than the daily average measurement of Table 2) could produce a temporary increase of the upper atmosphere temperature. However, such an increase in solar activity should also result in an increase of the CO Cameron band system emission brightness during orbit 983, which is not observed (see Table 2).

[52] *Breus et al.* [2004] have observed 50 to 60% higher electron temperatures correlated with the crustal magnetic fields. These authors associated this electron temperature increase with a population of hot electrons trapped at higher altitudes. This could explain the origin of the observed temperature increase of orbit 983, which would then be due to a change in the sources of the observed emission, rather than a true increase in neutral temperature. Indeed, we assumed in estimating these temperatures that photodissociative excitation of CO_2 was the main source for the CO Cameron band and the CO_2^+ ($B^2\Sigma^+$ - $X^2\Pi$) doublet emissions. If a significant population of hot electrons is present at higher altitudes, it may imply that electron impact dissociative excitation may also contribute to the observed emissions at high altitudes. Therefore it is better to consider these changes in the Martian dayglow in terms of variation of the scale heights of the emission, rather than of actual atmospheric temperatures. The measured scale height of the CO Cameron band system emission during orbit 983 is ~18.3 km, compared to the ~14 km average for all the orbits.

[53] It is somewhat surprising that the increase of the scale height of these emissions also occurs in the northern hemisphere at 180° east longitude, where no significant crustal field at 140 km is thought to be present (Figure 3). This suggests that the topology of the magnetic field (on the dayside) may be different than deduced from the mapping phase orbit of MGS (on the nightside) and be significantly extended at higher latitude than displayed Figure 3. In particular, the draping of the interplanetary magnetic field lines around the crustal fields could change significantly the motion of photoelectrons inside the Martian atmosphere at this particular local time and latitude region. New observations of the dayglow in the same conditions as orbit 983 are needed to resolve these questions, hopefully in coordination with ASPERA 3 in situ particle measurements.

4. Conclusion

[54] The SPICAM experiment on Mars Express is composed of UV and IR spectrographs dedicated to the observation of the Martian atmosphere and surface by stellar and solar occultations, nadir viewing, and limb viewing [*Bertaux et al.*, 2006]. Limb viewing observations are used to observe the Martian airglow [*Bertaux et al.*, 2005a, 2005b]. In this paper, a set of observations of the Martian dayglow obtained by SPICAM UV spectrometer between October 2004 and March 2005 are described and analyzed.

[55] The present coverage by this first major set of SPICAM dayglow measurements remains unfortunately rather sparse in terms of solar zenith angle, longitude, aerocentric longitude and latitude. Indeed, limb viewing observations of the dayglow imply a particular orientation of the spacecraft, and a special operational mode of SPICAM in order to get the best S/N ratio. The observations presented here constitute only 24 orbits, but represent more than 24,000 individual spectra with good S/N ratio for the most prominent emissions of the Martian dayglow.

[56] The main characteristics of the Martian dayglow are reevaluated 30 years after their last observation. In particular, a detailed comparison of these new observations with observations by Mariner 6 and 7 [*Barth et al.*, 1971] and Mariner 9 [*Barth et al.*, 1972] is performed. The CO ($a^3\Pi$ – $X^1\Sigma^+$) Cameron band system emission is significantly lower in intensity than measured by the earlier space missions. Moreover, the thermosphere temperature of 201 K derived from an average profile of the CO_2^+ ($B^2\Sigma^+$ - $X^2\Pi$) doublet emissions is significantly lower than the temperature derived in a similar way from Mariner 6, 7 and 9 observations, but are in reasonable agreement with more recent radio occultation and accelerometer measurements. The average scale height (~11.2 km) of the CO_2^+ ($B^2\Sigma^+$ - $X^2\Pi$) doublet emission is significantly lower than the scale height (~14 km) of the CO Cameron band system, which is likely due to a significant contribution of dissociative recombination of CO_2^+ to the Cameron band system emission above the peak emission altitude.

[57] The spectra measured by SPICAM display a feature at 276 nm that we suggest is the (0,6) band of the N_2 Vegard-Kaplan ($A^3\Sigma^+$ - $X^1\Sigma^+$) system. The intensity of this band is in good agreement with the calculations done by *Fox and Dalgarno* [1979] and *Fox et al.* [1977] as well as the N_2/CO_2 mixing ratios calculated by *Krasnopolsky* [2002] and *Fox* [2004b].

[58] The dominant emissions above the Martian exobase are Lyman α (due to the resonant scattering of sunlight by H

atoms) and 130.4 nm (due to resonant scattering of sunlight by O atoms). Both emissions vary with solar zenith angle and aerocentric longitude, which will be analyzed further in forthcoming investigations of the Martian corona.

[59] Finally, the orbit by orbit analysis of the scale height of the CO Cameron band system and the CO_2^+ ($B^2\Sigma^+$ - $X^2\Pi$) doublet indicates a potential effect of crustal magnetic fields on the Martian dayglow. During the only orbit in which the field of view of the SPICAM UVS passed above a large crustal magnetic field, a significant increase in the scale height of the CO Cameron band system emission is observed. We attribute this change to the influence of the crustal field on the transport of hot electrons within the Martian upper atmosphere [*Breus et al.*, 2004].

[60] A 2-year extension of the Mars Express mission has been recently approved. These new years of observation will allow us to test several tentative conclusions described here regarding the Martian dayglow, and, in particular, will significantly increase our present coverage of the Martian year.

Appendix A

A1. Description of the SPICAM UVS

[61] The optical scheme of the UV channel is displayed Figure 1 of *Bertaux et al.* [2006]. The light enters through a baffle, reflects from an off axis parabolic mirror, and is diffracted by a toroidal grating onto the intensifier and CCD. The CCD has 404 pixels along the spectral direction and 289 pixels along the spatial direction. A slit can be mechanically placed (or not) at the focal plane of the primary mirror. This slit was in place for all the dayglow measurements discussed in this paper. It is composed of two parts:

[62] 1. A 50 μm × 4.6 mm narrow part with a field of view (FOV) 0.02° wide by 1.9° long, projecting onto 200 lines of the CCD (a line of the CCD is defined as parallel to the spectral direction). The filled slit spectral resolution is equal to 1.5 nm (actually varying from 1 to 3 nm [see *Bertaux et al.*, 2006, Figure 13]).

[63] 2. A 500 μm × 2.2 mm wide part with a FOV 0.2° wide by 0.98° long, projecting onto 88 lines of the CCD. The filled slit resolution is only 6 nm, but this wide part provides 8 times the sensitivity of the narrow part of the slit.

[64] The scheme of the intensified CCD detector is displayed in Figure 2 of *Bertaux et al.* [2006]. The light reflected from the grating through the input windows which are composed of MgF_2, which is transparent at wavelengths >115 nm, and SiO_2, which is transparent at wavelengths >160 nm. The SiO_2 window covers only the portion of the CCD above 160 nm, in order to suppress the second order of the intense Lyman α emission line. The intensifier is composed of a photocathode, a microchannel plate (MCP), and a phosphor screen. The MCP high voltage can be adjusted such that its gain can vary by a factor ∼500. Fiber optics have been placed between the exit of the phosphor screen and the CCD. The CCD is divided into three parts along the spectral direction:

[65] 1. The center of the CCD receives the intensified light (between the 8th and the 391st pixels). The pixels are ordered from the largest wavelength (320 nm) down to the smallest wavelength (118 nm).

[66] 2. The 1st up to the 6th pixel do not receive any light from the intensifier and are used to measure the bias offset.

[67] 3. The pixels between the 398th and the 403rd measure the signal coming from a blind part of the detector and are used to measure the dark current from the detector.

[68] For telemetry limitations but also because of the time needed to read all the lines of the CCD, in normal observations only 5 adjacent parts of the CCD are read out. Each part is called a "spatial bin" and is constituted of 1, 2, 4, 8, 16 or 32 lines of the CCD following a preselected mode. For 10 of the observations described in this paper, the read part of the CCD was roughly centered on the spatial range, with two 32-pixel-line spatial bins corresponding to light from the narrow part of the slit, one 32-pixel-line spatial bin corresponding to light from both narrow and wide parts of the slit, and two 32-pixel-line spatial bins corresponding to light from the wide part of the slit. Thus each spatial bin covers a different region of the atmosphere, with a different spectral resolution and a different sensitivity. The rest of the observations use a binning of 16 pixel lines, with all the spatial bins receiving light from the narrow part of the slit. A typical observation of the dayglow during one MEX orbit lasts ∼20 min centered on the time when MEX is at the pericenter of its 259 km by 11,559 km (3.4 Mars Radii) polar orbit. This period is decomposed into ∼1200 consecutive individual sequences, each lasting one second, which are composed of 640 ms integration time and 360 ms reading and processing time. The length of the integration can be shortened if necessary, but was 640 ms for all the observations discussed here.

A2. Data Treatment

[69] The 5 spatial bins are read "spectel" (defined here as the sum of 32 or 16 pixels along the spatial direction at one spectral position along the CCD) by spectel, that is, 384 centered spectels, plus 6 spectels dedicated to the bias offset, plus 6 spectels dedicated to the dark current. During the reading, a supplementary voltage is applied, which is equivalent to adding a certain number of ADU (Analog to Digital Unit) to the measured signal. This offset ADU is variable from one spatial bin to another but can be reasonably supposed as constant for all the spectels along a given spatial bin. The average measured on the 6 bias offset spectels is then subtracted from all the centered and masked spectels of the spatial bin. The typical offset value is 34.1 ± 2.1 ADU/spectel.

[70] The main difficulty related to a good estimate of the dark current (DC) is its nonuniformity (DCNU) within the CCD. Dedicated observations to obtain a good image of the DCNU in the same conditions as airglow observations have been performed. During such observations the gain on the MCP is set to zero and the same region of the CCD with the same binning is used. Four observations of that type have been done for a binning of 16 lines and one for a binning of 32 (each observation being composed of 1200 consecutive spectra). The average DC intensity on the used pixels evolves linearly with respect to the average DC intensity measured on the masked pixels [see *Bertaux et al.*, 2006, section 4.3]. Therefore it is possible to normalize the DCNU measured on the used pixels by the DC measured on the masked pixels in order to obtain an idea of the non uniformity of

the DC on the CCD. It has been checked that this nonuniformity does not change significantly with time as well as with respect to the intensity of the DC by comparing the spectra obtained during each of these five dedicated observations as well as by comparing the DCNU measured during the four dedicated and similar observations (done within a period of 8 months). In the case of a 16 lines binning, an image of the normalized DCNU has been constructed by averaging the normalized DCNU measured during the 4×1200 sequences of observation of the four similar dedicated observations. In the case of a 32 lines binning, the image of the DCNU is built by averaging the 1200 spectra of the normalized DCNU obtained during the only dedicated observation with a binning of 32. For each observation of the airglow considered in this paper, we then subtract the corresponding image of the DCNU multiplied by the DC measured on the masked pixels during the integration time to be treated.

[71] During cruise phase, observations of stars indicated the presence of electronic noise generated by the reading of the CCD. This electronic noise is now relatively well characterized and has a peak intensity of only few ADU. We have developed several methods to subtract it. However, it appears that correcting typical dayglow measurements leads to the introduction of substantial errors in the resulting signal. Therefore no subtraction of this electronic read noise has been performed on the data analyzed here.

[72] Spectral calibration is done using an experimental calibration measured before the launch. This calibration has been successfully checked with respect to the thinnest and most intense emissions of the Martian dayglow (e.g., Lyman alpha at 121.6 nm and the CO_2^+ ($B^2\Sigma^+$ - $X^2\Pi$) ultraviolet doublet near 289 nm).

[73] The brightness calibration is done using a model curve for the number of ADU generated per photo-event with respect to the gain applied to the MCP. A photo-event is defined as a pulse of light in the phosphor of the intensifier following the creation of a photoelectron at the cathode of the intensifier. The assignment of the number of photo-events resulting from a given number of photons at the entrance of the spectrograph as a function of wavelength, is based on stellar calibration. Observations of stars well observed by other calibrated instruments (in particular, the IUE telescope) are regularly performed with the SPICAM UVS. The stellar signal measured is expressed in ADU as

$$N_{ADU}(\lambda) = Fs(\lambda) \times S_{eff}(\lambda) \times G \times d\lambda \times dt/0.9, \qquad (A1)$$

where λ is the wavelength, $N_{ADU}(\lambda)$ is the number of ADU measured at λ (in one spectel), $Fs(\lambda)$ is the observed signal at λ (in photons/cm^2/s/nm), G the gain of the MCP, $S_{eff}(\lambda)$ is the effective area at λ (in cm^2), $d\lambda$ = 0.543 nm is the wavelength interval covered by one spectel and dt is the time of integration. The coefficient 0.9 is here to take into account that the star is a point source, whereas the airglow is an extended source [see *Bertaux et al.*, 2006]. From equation (A1) and the observations of several bright UV stars (Zeta Puppis, Bet Cen, Eta Uma and Zeta Oph), we deduce S_{eff}, which is the blue curve in Figure 11 of *Bertaux*

et al. [2006]. A measurement above 302 nm and below 119 nm will have small signal/noise (S/N) ratio. The uncertainty on S_{eff} is less than 15%.

[74] The intensity for an extended source like the Martian dayglow can be expressed in photons/(cm^2 s sr nm) and the relation between the number of ADU per spectel and the spectral intensity is here expressed as

$$N_{ADU}(\lambda) = I(\lambda) \times S_{eff}(\lambda) \times G \times d\lambda \times dt \times dw \qquad (A2)$$

$I(\lambda)$ is the spectral intensity of the extended source and dw is the solid angle of one spectel of one spatial bin. Airglow intensity is usually expressed in Rayleighs, where one Rayleigh is equal to 10^6 photons/(cm^2 s ster) emitted into 4π steradians. Following equation (A2), the knowledge of S_{eff} from star calibration is sufficient to calibrate any dayglow observation.

[75] The result is a calibrated spectral signal in Rayleigh/nm versus wavelength. The extraction of the brightness of different emission lines can be done following two different approaches:

[76] 1. Using the Point Spread Function (PSF) of the instrument, which is the spectral form of an ideally spectrally thin signal observed by SPICAM. Such a PSF is convolved with a theoretical spectrum to fit the measured signal. So far, we have not obtained an instrumental measurement of the PSF for the whole wavelength range and therefore cannot safely use this method of analysis.

[77] 2. Directly integrating the measured signal between two wavelengths chosen in order to fully cover the spectral range in SPICAM of the emission line. This method is robust, but does not allow the separation of two emission lines spectrally too close together.

[78] For both methods of integration, we also estimate a background due to scattered light inside the spectrograph and to overlap by nearby emission lines. The method used to evaluate this background is a simple interpolation of the measured signal around the spectral range of the targeted emission line. For the results presented here, we provide the result of the second method and therefore consider only clearly separated emission lines and band systems.

[79] During each orbit ~1200 individual and consecutive spectra are recorded. The integration of emission intensity has been done either by averaging consecutive spectra during one orbit (e.g., within a chosen altitude range) or by averaging all spectra constrained in other ways (e.g., from all orbits within a certain range of Solar Zenith Angle (SZA), Solar longitude (Ls) or altitude). The second method typically provides a much better S/N ratio (a spectrum can be obtained from 1000 individual spectra) but has limited latitudinal and longitudinal resolution. In the following, the dependencies of key emissions with respect to SZA, Ls and altitude are deduced using the second method, whereas dependencies of the emissions with respect to latitude and longitude are derived using the first method.

[80] Brightness uncertainties are estimated in the following way:

$$S_{ADU} = DC_{ADU} + L_{ADU} + Offset,$$

where S_{ADU} is the total observed signal, DC_{ADU} is the dark current ($DC_{ADU} = N_{dc}/G$, where N_{dc} is the number of

electrons due to the dark current), L_{ADU} is the dayglow signal ($L_{ADU} = K \times n_{phe}$ where K is the number of ADU per photo-event and n_{phe} is the number of photo-events), and Offset is assumed to be a well-known constant without any variance. The uncertainty (in ADU) of one measured atmospheric signal for one spectel is then: $\sigma(L_{ADU}) = (DC_{ADU}/G + 2 \times K \times L_{ADU} + R_0^2)^{1/2}$ where R_0 is associated to the electronic noise ($R_0 = 1$ ADU). The factor 2 in front of $K \times L_{ADU}$ is here to take into account the particular pulse height distribution of the photo-events [*Sandel and Broadfoot*, 1986].

[81] During some observations we occasionally notice strong signals associated with stray light. In particular, some spectra obtained in narrow part of the slit display two very intense peaks with respect to dayglow emission intensities centered on 132 and 143 nm or a very broad peak centered on 250 nm [see *Bertaux et al.*, 2006, Figure 17]. Such features are clearly not associated with atmospheric emissions because of their intensity and their variation with altitude and Solar Zenith Angle. The origin of this stray light is thought to be due to light diffusing inside the input windows (see explanations section 4.4 of *Bertaux et al.* [2006]). This light enters through the wide part of the slit and therefore may be 10 times more intense than the one passing through the narrow part of the slit. In some cases, the wide part of the slit can observe a region of the Martian atmosphere which is much brighter than the atmosphere observed by the narrow part of the slit, so that the relative contribution is even larger. We believe that light passing through the wide part of the slit and diffusing through the MgF_2 window produces the large bump centered at 250 nm. Such a spectral feature corresponds to the diffused image of the solar flux reflected by Rayleigh scattering in the low Martian atmosphere [*Bertaux et al.*, 2006, Figure 17]. In the same way, the two features at 132 and 143 nm would be due to specular reflections inside the SiO_2 window and in particular at the edge of the window. We chose to exclude all orbits during which one of these features is clearly identified during at least one sequence obtained with a FOV above 100 km in altitude.

References

Acuña, M. H., et al. (2001), Magnetic field of Mars: Summary of results from he aerobraking and mapping orbits, *J. Geophys. Res.*, *106*, 23,403–23,417.

Anderson, D. E., and C. W. Hord (1971), Mariner 6 and 7 Ultraviolet Spectrometer Experiment: Analysis of Hydrogen Lyman-Alpha data, *J. Geophys. Res.*, *76*, 6666–6673.

Barth, C. A., C. W. Hord, J. B. Pearce, K. K. Kelly, G. P. Anderson, and A. I. Stewart (1971), Mariner 6 and 7 Ultraviolet Spectrometer Experiment: Upper atmosphere data, *J. Geophys. Res.*, *76*, 2213–2227.

Barth, C. A., A. I. Stewart, C. W. Hord, and A. L. Lane (1972), Mariner 9 Ultraviolet Spectrometer Experiment: Mars airglow spectroscopy and variations in Lyman Alpha, *Icarus*, *17*, 457–462.

Bertaux, J. L., et al. (2000), The study of the Martian atmosphere from top to bottom with SPICAM Light on Mars Express, *Planet. Space Sci.*, *48*, 1303–1320.

Bertaux, J.-L., et al. (2005a), First observation of nightglow in the upper atmosphere of Mars: The NO bands in UV and implications for atmospheric transport, *Science*, *307*, 566–569.

Bertaux, J.-L., F. Leblanc, O. Witasse, E. Quémerais, J. Lilensten, A. S. Stern, B. Sandel, and O. Korablev (2005b), Discovery of aurora on Mars, *Nature*, *435*, 790–794.

Bertaux, J.-L., et al. (2006), SPICAM on board Mars Express: Instruments, operations, observing mode, and overview typical results, *J. Geophys. Res.*, doi:10.1029/2006JE002690, in press.

Bougher, S. W., S. Engel, R. G. Roble, and B. Foster (2000), Comparative terrestrial planet thermospheres: 3. Solar cycle variation of global structure and winds at solstices, *J. Geophys. Res.*, *105*, 17,669–17,689.

Bougher, S. W., D. P. Hinson, J. M. Forbes, and S. Engel (2001), MGS Radio Science electron density profiles and implications for the neutral atmosphere, *Geophys. Res. Lett.*, *28*, 3091–3094.

Bougher, S. W., S. Engel, D. P. Hinson, and J. R. Murphy (2004), MGS Radio Science electron density profiles: Interannual variability and implications for the Martian neutral atmosphere, *J. Geophys. Res.*, *109*, E03010, doi:10.1029/2003JE002154.

Brain, D. A., F. Bagenal, M. H. Acuña, J. E. P. Connerney, D. H. Crider, C. Mazelle, D. L. Mitchell, and N. F. Ness (2002), Observations of low-frequency electromagnetic plasma waves upstream from the Martian shock, *J. Geophys. Res.*, *107*(A6), 1076, doi:10.1029/2000JA000416.

Breus, T. K., A. M. Krymskii, D. H. Crider, N. F. Ness, D. Hinson, and K. K. Barashyan (2004), Effect of the solar radiation in the topside atmosphere/ionosphere of Mars: Mars Global Surveyor observations, *J. Geophys. Res.*, *109*, A09310, doi:10.1029/2004JA010431.

Chassefière, E., and F. Leblanc (2004), Mars atmospheric escape and evolution: Interaction with the solar wind, *Planet. Space Sci.*, *52*, 1039–1058.

Conway, R. R. (1981), Spectroscopy of the Cameron bands in the Mars airglow, *J. Geophys. Res.*, *86*, 4767–4775.

Cossart, D., and C. Cossart-Magos (1996), A new spectral emission source of rotationally cooled molecular ions: Application to supersonic expansions of CO and CO_2 gases, *Chem. Phys. Lett.*, *250*, 128–136.

Dalgarno, A., and M. B. McElroy (1970), Mars: Is nitrogen present?, *Science*, *170*, 167–168.

Durrance, S. T. (1981), The carbon monoxide fourth positive bands in the Venus dayglow: 1. Synthetic spectra, *J. Geophys. Res.*, *86*, 9115–9124.

Eastes, R. W., R. E. Huffman, and F. J. Leblanc (1992), NO and O_2 ultraviolet nightglow and spacecraft glow from the S3-4 satellite, *Planet. Space Sci.*, *40*, 481–493.

Feldman, P. D., E. B. Burgh, S. T. Durrance, and A. F. Davidsen (2000), Far-ultraviolet spectroscopy of Venus and Mars at 4A resolution with the Hopkins Ultraviolet Telescope on Astro-2, *Astrophys. J.*, *538*, 395–400.

Forbes, J. M., A. F. C. Bridger, S. W. Bougher, M. E. Hagan, J. L. Hollingsworth, G. M. Keating, and J. Murphy (2002), Nonmigrating tides in the thermosphere of Mars, *J. Geophys. Res.*, *107*(E11), 5113, doi:10.1029/2001JE001582.

Fox, J. L. (1992), Airglow and aurora in the atmospheres of Venus and Mars, in *Venus and Mars: Atmospheres, Ionospheres, and Solar Wind Interactions*, *Geophys. Monogr. Ser.*, vol. 66, edited by J. G. Luhmann, M. Tatrallyay, and R. O. Pepin, pp. 191–222, AGU, Washington, D .C.

Fox, J. L. (2004a), CO_2^+ dissociative recombination: A source of thermal and nonthermal C on Mars, *J. Geophys. Res.*, *109*, A08306, doi:10.1029/2004JA010514.

Fox, J. L. (2004b), Response of the Martian thermosphere/ionosphere to enhanced fluxes of solar soft X rays, *J. Geophys. Res.*, *109*, A11310, doi:10.1029/2004JA010380.

Fox, J. L., and A. Dalgarno (1979), Ionization, luminosity, and heating of the upper atmosphere of Mars, *J. Geophys. Res.*, *84*, 7315–7333.

Fox, J. L., and A. Dalgarno (1981), Ionization, luminosity, and heating of the upper atmosphere of Venus, *J. Geophys. Res.*, *86*(A2), 629–639.

Fox, J. L., A. Dalgarno, E. R. Constantinides, and G. A. Victor (1977), The nitrogen dayglow on Mars, *J. Geophys. Res.*, *82*, 1615–1616.

Gutchek, R. A., and E. C. Zipf (1973), Excitation of the CO fourth positive system by the dissociative recombination of CO_2^+ ions, *J. Geophys. Res.*, *78*, 5429–5436.

Hanson, W. B., S. Satani, and D. R. Zuccaro (1977), The Martian ionosphere as observed by the Viking retarding potential analyzers, *J. Geophys. Res.*, *82*, 4351–4363.

Hantsch, M. H., and S. J. Bauer (1990), Solar control of the Mars ionosphere, *Planet. Space Sci.*, *38*, 539–542.

Keating, G. M., et al. (1998), The structure of the upper atmosphere of Mars: In-situ accelerometer measurements from Mars Global Surveyor, *Science*, *279*, 1672–1676.

Keating, G. M., M. Theriot, R. Tolson, S. Bougher, F. Forget, and J. Forbes (2003), Global measurement of the Mars upper atmosphere: In situ accelerometer measurements from Mars Odyssey 2001 and Mars Global Surveyor, Proc. *Lunar Planet. Sci. Conf. 36th*, abstract 1142.

Kerzhanovich, V. V. (1977), Mars 6: Improved analysis of the descent module measurements, *Icarus*, *30*, 1−25.

Krasnopolsky, V. A. (1982), Atomic carbon in the atmospheres of Mars and Venus (in Russian), *Kosmicheskie Issled.*, *20*, 595−603, (*Cosmic Res.*, Engl. Transl., *20*, 430−437, 1983.)

Krasnopolsky, V. A. (2002), Mars' upper atmosphere and ionosphere at low, medium, and high solar activities: Implications for evolution of water, *J. Geophys. Res.*, *107*(E12), 5128, doi:10.1029/2001JE001809.

Krasnopolsky, V. A., and P. D. Feldman (2001), Detection of molecular hydrogen in the atmosphere of Mars, *Science*, *294*, 1914−1917.

Krasnopolsky, V. A., and P. D. Feldman (2002), Far ultraviolet spectrum of Mars, *Icarus*, *160*, 86−94.

Krasnopolsky, V. A., and G. R. Gladstone (2005), Helium on Mars and Venus: EUVE observations and modeling, *Icarus*, *176*, 395−407.

Krasnopolsky, V. A., M. J. Mumma, and G. R. Gladstone (1998), Detection of atomic deuterium in the upper atmosphere of Mars, *Science*, *280*, 1576−1580.

Krymskii, A. M., T. K. Breus, N. F. Ness, M. H. Acuña, J. E. P. Connerney, D. H. Crider, D. L. Mitchell, and S. J. Bauer (2002), Structure of the magnetic field fluxes connected with crustal magnetization and topside ionosphere at Mars, *J. Geophys. Res.*, *107*(A9), 1245, doi:10.1029/2001JA000239.

Levine, J. S., D. S. McDougal, D. E. Anderson, and E. S. Barker (1978), Atomic hydrogen on Mars: Measurements at solar minimum, *Science*, *200*, 1048−1051.

Luhmann, J. G., and J. U. Kozyra (1991), Dayside pick-up oxygen in precipitation at Venus and Mars: Spatial distribution, energy deposition and consequences, *J. Geophys. Res.*, *96*, 5457−5467.

Lundin, R., et al. (1989), First measurements of the ionospheric plasma escape from Mars, *Nature*, *341*, 609−612.

Lundin, R., et al. (2004), Solar wind-induced atmospheric erosion at Mars: First results from ASPERA-3 on Mars Express, *Science*, *305*, 1933−1936.

Ma, Y., A. F. Nagy, I. V. Sokolov, and K. C. Hansen (2004), Three-dimensional, multispecies, high spatial resolution MHD studies of the solar wind interaction with Mars, *J. Geophys. Res.*, *109*, A07211, doi:10.1029/2003JA010367.

Magalhaes, J. A., J. T. Schofield, and A. Seiff (1999), Results of the Mars Pathfinder atmospheric structure investigation, *J. Geophys. Res.*, *104*, 8943−8955.

McElroy, M. B., and J. C. McConnell (1971), Atomic carbon in the atmospheres of Mars and Venus, *J. Geophys. Res.*, *76*, 6674−6690.

Mitchell, D. L., R. P. Lin, C. Mazelle, H. Rème, P. A. Cloutier, J. E. P. Connerney, M. H. Acuña, and N. F. Ness (2001), Probing Mars' crustal magnetic field and ionosphere with the MGS Electron Reflectometer, *J. Geophys. Res.*, *106*, 23,419−23,427.

Nier, A. O., and M. B. McElroy (1977), Composition and structure of Mars' upper atmosphere: Results from the neutral mass spectrometers on Viking 1 and 2, *J. Geophys. Res.*, *82*, 4341−4349.

Pätzold, M., S. Tellmann, B. Häusler, D. Hinson, R. Schaa, and G. L. Tyler (2005), A sporadic third layer in the ionosphere of Mars, *Science*, *310*, 837−839.

Paxton, L. J. (1985), Pioneer Venus orbiter ultraviolet spectrometer limb observations: Analysis and interpretation of the 166- and 156-nm data, *J. Geophys. Res.*, *90*, 5089−5096.

Paxton, L. J., and D. E. Anderson (1992), Far ultraviolet remote sensing of Venus and Mars, in *Venus and Mars: Atmospheres, Ionospheres, and Solar Wind Interactions, Geophys. Monogr. Ser.*, vol. 66, edited by J. G. Luhmann, M. Tatrallyay, and R. O. Pepin, pp. 113−189, AGU, Washington, D. C.

Purucker, M., et al. (2000), An altitude-normalized magnetic map of Mars and its interpretation, *Geophys. Res. Lett.*, *27*, 2449−2452.

Rottman, G. J., and H. W. Moos (1973), The ultraviolet (120−190 nm) spectrum of Venus, *J. Geophys. Res.*, *78*, 8033−8084.

Sandel, B. R., and A. L. Broadfoot (1986), Statistical performance of the intensified charge coupled device, *Appl. Opt.*, *25*, 4135−4140.

Schofield, J. T., J. R. Barnes, D. Crisp, R. M. Haberle, S. Larsen, J. A. Magalhães, J. R. Murphy, A. Seiff, and G. Wilson (1997), The Mars Pathfinder atmospheric structure investigation/meteorology (ASI/MET) experiment, *Science*, *278*, 1752−1758.

Seiff, A., and D. B. Kirk (1977), Structure of the atmosphere of Mars in summer in mid-latitudes, *J. Geophys. Res.*, *82*, 4364−4378.

Stewart, A. L. (1972), Mariner 6 and 7 Ultraviolet Spectrometer Experiment: Implications of CO_2^+, CO and O airglow, *J. Geophys. Res.*, *77*, 54−68.

Stewart, A. I., C. A. Barth, C. W. Hord, and A. L. Lane (1972), Mariner 9 Ultraviolet Spectrometer Experiment: Structure of Mars' upper atmosphere, *Icarus*, *17*, 469−474.

Strickland, D. J., G. E. Thomas, and P. R. Sparks (1972), Mariner 6 and 7 Ultraviolet Spectrometer Experiment: Analysis of the OI 1304−1356−A emissions, *J. Geophys. Res.*, *77*, 4052−4068.

Strickland, D. J., G. E. Thomas, and P. R. Sparks (1973), Mariner 9 Ultraviolet Spectrometer Experiment: Mars atomic oxygen 1304−A emissions, *J. Geophys. Res.*, *78*, 4547−4559.

Tracadas, P. W., M. T. Zuber, D. E. Smith, and F. G. Lemoine (2001), Density structure of the upper thermosphere of Mars from measurements of air drag on the Mars Global Surveyor spacecraft, *J. Geophys. Res.*, *106*, 23,349−23,357.

Wang, J.-S., and E. Nielsen (2004), Evidence for topographic effects on the Martian ionosphere, *Planet. Space Sci.*, *52*, 881−886.

Witasse, O. (2000), Modélisation des ionospheres planétaires et de leur rayonnement: La Terre et Mars, Ph.D. thesis, Univ. Joseph Fourier, Grenoble, France, July.

Withers, P., S. W. Bougher, and G. M. Keating (2004), The effects of topographically-controlled thermal tides in the Martian upper atmosphere as seen by the MGS accelerometer, *Icarus*, *164*, 14−32.

————————————
J.-L. Bertaux, J. Y. Chaufray, and F. Leblanc, Service d'Aéronomie du CNRS/IPSL, BP 3 Reduit de Verrières, F-91371 Verrières-le-Buisson, France. (francois.leblanc@aerov.jussieu.fr)

J. Lilensten, Laboratoire de Planétologie de Grenoble, Grenoble, France.
O. Witasse, ESA-ESTEC, Noordwijk, 2200 AG, Netherlands.